Pulsed laser-induced heating of mineral phases: Implications for Laser-Induced Breakdown Spectroscopy combined with Raman spectroscopy

Amaury Fau, Olivier Beyssac, Michel Gauthier, P-Y. Meslin, Agnes Cousin, K. Benzerara, Sylvain Bernard, Jean-Claude Boulliard, Olivier Gasnault, Olivier Forni, et al.

Pulsed laser-induced heating of mineral phases: Implications for Laser-Induced Breakdown Spectroscopy combined with Raman spectroscopy

Fau A. [a,*], Beyssac O. [a,*], Gauthier M. [a], Meslin P.Y. [b,c], Cousin A. [b,c], Benzerara K. [a], Bernard S. [a], Boulliard J.C. [a], Gasnault O. [b,c], Forni O. [b,c], Wiens R.C. [d], Morand M. [a], Rosier P. [a], Garino Y. [a], Pont S. [a], Maurice S. [b,c]

[a] *Sorbonne Université, Muséum National d'Histoire Naturelle, CNRS, UMR 7590, Institut de Minéralogie, de Physique des Matériaux et de Cosmochimie, Paris, France*
[b] *Université de Toulouse, UPS-OMP, Toulouse, France*
[c] *Institut de Recherche en Astrophysique et Planétologie, CNRS, UMR 5277, Toulouse, France*
[d] *Los Alamos National Laboratory, Los Alamos, NM, USA*

[*] Corresponding authors.
Email address:
amaury.fau@upmc.fr
olivier.beyssac@upmc.fr

Keywords:
SuperCam
Laser-induced breakdown spectroscopy
Raman spectroscopy
Pulsed laser heating
Time-resolved spectroscopy

For Spectrochimica Acta B: Atomic Spectroscopy

ABSTRACT

Laser-Induced Breakdown Spectroscopy (LIBS) and Raman spectroscopy are complementary techniques providing respectively chemical and structural information on the sample target. These techniques are increasingly used together in Earth and Planetary sciences, and often together. LIBS is locally destructive for the target, and the laser-induced effects due to LIBS laser shots on the structure and on the Raman fingerprint of a set of geological samples relevant to Mars are here investigated by Raman spectroscopy and electron microscopy. Experiments show that the structure of samples with low optical absorption coefficients is preserved as well as the structural information carried by Raman spectra. By contrast, minerals with high optical absorption coefficient can be severely affected by LIBS laser shots with local amorphization, melting and/or phase transformation. Thermal modelling shows that the temperature can reach several thousands of degrees at the surface for such samples during a LIBS laser shot, but decreases rapidly with time and in space. In 2020, NASA Mars 2020 mission will send a rover equiped with a combined LIBS/Raman instrument for remote analysis (SuperCam) as well as fine-scale instruments for X-ray fluorescence (Planetary Instrument for X-Ray Lithochemistry - PIXL) and deep UV Raman spectroscopy (Scanning Habitable Environments with Raman and Luminescence for Organics and Chemicals - SHERLOC) for proximity science. We discuss the implications of our results for the operation of these instruments and show that (i) the SuperCam analytical footprint for Raman spectroscopy is many times larger than the LIBS crater, minimizing any effects and (ii) SHERLOC and PIXL analysis may be affected if they analyze within a LIBS crater created by SuperCam LIBS.

1. Introduction

Laser-induced breakdown spectroscopy (LIBS) is a technique detecting atomic composition of solid and fluids by analyzing the light emitted by a plasma created by laser ablation of the sample. Raman spectroscopy is a vibrational spectroscopy technique detecting the molecular structure of solids and fluids based on the analysis of the energy change of a laser interacting with a sample due to non-elastic scattering. The complementary and versatility of these methods make them increasingly used conjointly in many scientific fields like Earth and Planetary Sciences or Art and Archeology. Because the two techniques use a similar instrumental architecture based on the same principal components (a laser, a spectrometer and a detector), several combined LIBS-Raman customized setups have been elaborated. Some setups were designed for analysis at the microscale [1,2] while other setups were developed for remote analysis [3–8] in particular for field measurements. Notably, most of these instruments were developed with the motivation of designing a compact LIBS-Raman instrument for future planetary exploration.

In 2020, the NASA Mars 2020 mission will send a new rover to Mars with a scientific payload dedicated to the *in situ* characterization of targeted rocks and to trace putative organic traces of life [9]. Among these instruments, SuperCam is a multitool remote sensing instrumental suite offering five complementary techniques [10]. (1) LIBS with a design inspired from the successful Curiosity rover instrument ChemCam [11–15]. LIBS will offer the possibility to document, at remote distances, the chemical composition of major and many trace elements within a spot of a few hundreds of micrometers in diameter. (2) A time-resolved (TR) Raman and luminescence spectrometer with a substantially larger analytical footprint than LIBS and (3) a visible and infrared (VISIR) spectrometer [16], also with a larger footprint than the LIBS, will together give mineralogical information complementing the chemical information provided by LIBS. In addition, SuperCam will include (4) a microphone [17] and (5) a high-resolution color imager [18] for context imagery. The Mars 2020 mission is also equipped with a deep UV Raman instrument called Scanning Habitable Environments with Raman & Luminescence for Organics & Chemicals (SHERLOC) and a X-ray fluorescence instrument called Planetary Instrument for X-ray Lithochemistry (PIXL) which have analytical footprints smaller or in the range of the LIBS crater and are made for analyses at fine spatial scales for proximity science.

LIBS is destructive for the target surface over a small area because the high-energy pulsed laser is focused to ablate and generate the plasma required for LIBS analysis. However, the surface and the volume impacted are relatively small [11]. In contrast, Raman spectroscopy works best on pristine surfaces of non-structurally-altered minerals. In practice, Raman spectra are generally always taken with care to avoid laser irradiance that would modify or damage the molecular structure of the surface. Overall, it thus appears critical for all studies combining these methods in the same analytical footprint to assess whether LIBS laser shots are detrimental to the target mineral structure, and hence to Raman signatures. Moreover, this assessment is needed for different target mineralogies and different analytical conditions under which LIBS analyses are performed such as pressure and composition of the atmosphere or the number of shots.

Here, we compare the Raman signatures of a selection of various minerals already observed on Mars by orbital or *in situ* investigations, before and after LIBS shots. These minerals cover a wide range of physical properties controling their behaviour under laser irradiation like optical absorption or thermal diffusivity. The surface of LIBS-induced craters was imaged and characterized at the microscale using scanning electron microscopy (SEM). Further investigations down to the nanoscale were conducted using transmission electron microscopy (TEM) on focused ion beam (FIB) sections for a hematite sample exhibiting LIBS laser-induced modifications. Results are then compared to calculations of the thermal heating due to the laser pulses and finally integrated in a general discussion about the combined use of LIBS and Raman spectroscopy, in particular for the use of the instruments of the Mars 2020 mission.

2. Methodology

2.1. LIBS

The LIBS analyses were performed at the Institut de Recherche en Astrophysique et Planétologie (IRAP, Toulouse, France), using one of two existing MSL ChemCam replicas. This instrument is composed of the ChemCam Mast Unit Engineering Qualification model placed into a climate-controlled chamber at 263K. This unit consists mainly of the laser and the telescope, and is combined with the ChemCam Body Unit Engineering model including the spectrometers and detectors. A Nd : KGW laser beam delivering an energy of 24 mJ (11 mJ at the sample surface) at 1067 nm, with a pulse duration of 6 ns at full width at half maximum (FWHM) and a 3 Hz repetition rate, is focused onto a target in a laser spot of

around 400±100 micrometers in diameter [15,19,20]. Distribution of the laser energy is not perfectly gaussian yielding LIBS crater with triangular shape visible on some targets. The plasma light is collected by a telescope and is distributed to 3 spectrometers to generate the LIBS spectra: ultra-violet (UV) 240-340 nm, visible (VIS) 380-470 nm and visible-infrared (VISIR) 480-950 nm. More details on the experimental setup at IRAP may be found in Cousin *et al.* [21] and Rapin *et al.* [22].

All measurements were done at a distance of 1670 mm, which is roughly the distance to the calibration target on the MSL Curiosity rover. Due to the laser slight divergence, there is a linear increase of the laser spot diameter with the target distance. This causes a decrease of the LIBS laser irradiance and consequently a decrease of possible effects on mineral structure with distance. Moreover, in order to investigate a possible influence of the atmospheric conditions on the LIBS effect on mineral structure, various environmental conditions have been tested by carrying out the LIBS analyses under (1) Earth atmosphere, (2) vacuum (pressure below 10^{-3} mbar) and (3) Martian atmosphere (6 mbar of 96% CO_2, 2.6% N_2 and 1.4% Ar). The number of laser shots was also tested by performing series of 5, 10, 20, 30, 100 or 150 shots depending on the session and/or target. Thirty shots is the nominal number of laser shots for ChemCam analyses on Mars and this will likely be the same for SuperCam. Unless otherwise specified, measurements in a Martian atmosphere using 30 LIBS shots series were used in this study.

2.2. Scanning Electron Microscopy

The morphology and texture of LIBS craters were observed by SEM. All images using backscattered electrons (BSE) were obtained using the TESCAN VEGA II LSU scanning electron microscope (SEM) of the Electron Microscopy and Microanalyses Technical Platform of the Museum National d'Histoire Naturelle (Paris, France). This microscope was run under environmental conditions at an accelerating voltage of 15 kV and under a residual nitrogen pressure varying from 14 Pa to 25 Pa in the analysis chamber. This allowed us to analyze samples without prior deposition of metal or carbon coating. This was particularly interesting since coatings like amorphous carbon or gold are very limiting for Raman spectroscopy as they not only absorb incident laser light and the backscattered signal, but they also generate important fluorescence background masking the Raman signal. In addition, the coating of non-polished samples with topographic variations such as a LIBS crater at the

surface of a sample, is extremely difficult to remove mechanically by polishing without damaging the sample.

Because hematite has a high electrical conductivity, additionnal SEM observations were performed on uncoated hematite using a secondary electron or secondary ion detector (SESI) on a Zeiss Neon40EsB CrossBeam instrument at Institut de Minéralogie, de Physique des Matériaux et de Cosmochimie (IMPMC, Paris, France). Images were obtained with a working distance of 5.5 mm and an accelerating voltage of 5 kV.

2.3. Raman spectroscopy

All samples were first analyzed using a continuous-wave (CW) Raman microspectrometer Renishaw InVia Reflex for point analyses and Raman mapping when needed. Measurements were performed using a green 532 nm solid-state laser focused on the sample through a Leica DM2500 microscope with a long-working distance 50X objective (NA=0.55). This configuration yielded a horizontal resolution of ≈1-2 µm for a laser power delivered at the sample surface set at less than 1 mW using neutral density filters to prevent irreversible thermal damages. This corresponds to a laser irradiance in the range of 0.3-1.3 10^9 $W.m^{-2}$. All measurements were performed with a circularly polarized laser using a ¼-wave plate placed before the microscope in order to minimize polarization effects. The Raman signal was dispersed by a grating with 2400 lines/mm and the signal was analyzed with a RENCAM CCD detector. For Raman mapping and the acquisition of hyperspectral maps, the sample was moved with an appropriate step size using a XYZ Renishaw motorized stage. Laser focus was optimized by correcting topographic variation prior to analysis (surface mode using the Renishaw Wire 4.3 software) and all maps were processed using the Wire 4.3 software. More about Raman mapping can be found in Bernard *et al.* [23]. All measurements were performed at room temperature and spectra were recorded directly on the raw samples without any preparation.

All samples were also analyzed using a custom time-resolved Raman and luminescence spectrometer described by Beyssac *et al.* [24]. This instrument includes a Raman microscope (micro TR Raman) as well as a telescope (remote TR Raman) in a configuration similar to the SuperCam instrument. The laser is a nanosecond (1.2 ns FWHM, 1mJ per pulse) pulsed DPSS laser operating at 532 nm with a 10 to 2000 Hz repetition rate. In the microscopy setting, the laser is focused at the sample surface through a microscope objective (MPlan Apo Mitutoyo 20X, NA= 0.42) and the Raman signal is collected in the backscattering geometry. In the

micro TR Raman, the laser is circularly polarized thanks to a ¼-wave plate placed before the microscope in order to minimize polarization effects. In the remote setting, the laser is collimated at the sample surface 8 m from the telescope Schmidt plate on a spot of ≈6 mm diameter, and the Raman signal is collected by a conventional Schmidt-Cassegrain telescope (Celestron-C8 202 mm diameter Schmidt plate) on a spot of ≈6 mm diameter co-aligned with the laser spot. The laser is linearly polarized in the remote TR Raman as for SuperCam and the possible polarization effects on the relative intensity of the Raman peaks are not investigated here. In both settings, a Notch filter cuts off the Rayleigh scattering at ≈90 cm^{-1} and the signal is collected by an optical fiber and sent into a modified Czerny-Turner spectrometer (Princeton IsoPlane 320) coupled with an intensified Princeton PIMAX4 ICCD camera. The fine control of both time delay and gating time of the camera allows sub-nanosecond time resolution experiments thanks to an accurate synchronization between the laser pulse and the ICCD. This spectrometer has three motorized gratings which can be selected depending on the spectral window and resolution requested for the experiment. Irradiance associated with a pulsed laser can be roughly estimated as $Q/(\tau S)$, with $Q=P/f$ being the laser energy per pulse, P being the time-integrated laser power measured at the surface of the sample, f the laser repetition rate, τ the pulse duration, and S the surface of the laser spot on the sample. In both micro and telescopic configurations, irradiance was set at $\approx 10^{10}$ $W.m^{-2}$ which is conservative even in the case of absorbing minerals (see discussion below). In remote TR Raman we use a 100 ns ICCD gate similar to that used with SuperCam and centered on the laser pulse (1.2 ns pulse for the laboratory instrument versus 4 ns for SuperCam).

Presentation and discussion of the data is focused on the 30 LIBS laser shots unless specified because we did not oberve any significant difference in the Raman spectra collected from the craters with other shots number for a given sample. For the micro TR Raman data, we documented the effect of LIBS laser shots on the mineral structure and Raman signature. For this purpose, we compared the intensity ratios of the Raman signal over the background signal between LIBS-ablated and non-ablated areas as qualitative proxies for the LIBS effect on the Raman signature. Note that the laser was systematically focused at the sample surface within the crater cavity or on the pristine surfaces. The Raman signal was calculated based on the most intense Raman peak, specific to each sample, *i.e.* $R_{signal}=(I_{signal}(in))/(I_{signal}(out))$ taken over a range of 60 cm^{-1} ([-30,+30] cm^{-1}) around the maximum of intensity, where *in* stands for inside the LIBS crater, and *out* for outside. The background signal was calculated based on

the spectral range close to the most intense Raman peak, where no other Raman peak is present (the ranges are given in the Table 2). It is calculated by summing the intensity of each pixel in this spectral range, *i.e.* $R_{bkg}=(\sum[I(in)])/(\sum[I(out)])$.

2.4. FIB – TEM

In order to further characterize the mineralogical transformations induced by the LIBS shots on the hematite sample down to the nanometer-scale, TEM analyses were performed. For this purpose, an electron-transparent foil was cut through a 30-shots LIBS crater to observe the top five micrometers from the surface of the crater. First, the crater was located with a less than 10-nm positional accuracy using the FIB-SEM capabilities of a Zeiss dual FIB-NEON 40EsB operating at 30 keV and 10 nA at IMPMC (Paris, France). Second, a platinum strap, measuring around 100 nm in thickness was deposited onto the region of interest of the sample by electron-beam assistance before a Ga^+-beam assisted deposition of a second platinum strap measuring ≈1µm in thickness. Third, the focused Ga^+ beam operating at ≈10 nA excavated the sample from both sides of the Pt layer to a depth of ≈5 µm. Then, the foil was transferred to a copper grid and further thinned down to a thickness <100 nm using a Ga+ beam current of 100 pA. This method is further detailed by Bernard *et al.* [25] and Benzerara *et al.* [26]. The FIB foil was analyzed using a JEOL 2100F field emission gun transmission electron microscope (FEG-TEM) operated at 200 kV. These analyses provided 1) bright-field images with a sub-nm spatial resolution with contrast mostly due to diffraction in the present case where crystalline phases are present; 2) electron diffraction patterns providing crystallographic information and 3) elemental composition at the nm-scale.

2.5. Samples

Table 1 lists minerals and rocks used for this study and summarizes the main information for each target. Most minerals were obtained from the Collection de Minéralogie at Sorbonne Université (Paris, France). The majority of the samples are natural, either single crystals or polycrystalline aggregates, but a few of them are synthetic powders and were used as pressed pellets. This selection of minerals and rocks includes silicates (amethyst, sandstone, albite, olivine, orthopyroxenite, oligoclase and andesine), carbonates (calcite and hydromagnesite), phosphates (fluor-hydroxyapatite and hydroxyapatite), sulfates (two samples of gypsum: one as a single-crystal, the other in the form of powder pellet), two samples rich in graphitic carbon (a graphite and a coal) and a variety of oxides (pyrite, ilmenite and hematite).

The two phosphates were synthetic and were produced at the CIRIMAT laboratory (Toulouse, France). Hydroxyapatite (apatite OH) was obtained by precipitation [27]. Fluorination of the hydroxyapatite (apatite FOH) was obtained by placing NH_4F salt at the entrance of an alumina tube heated at 1173K under argon gas flow for 1 h in a tubular furnace. The obtained powders were then pressed into pellets of 13 mm diameter. The structure and the purity of these two apatites were verified by X-ray diffraction and infrared spectroscopy.

Most samples were not previously processed and LIBS was performed directly on the raw sample surfaces to be as close as possible to the analysis conditions on Mars [22]. For some of the samples with highly reflecting surfaces (olivine, orthopyroxenite, pyrite, hematite and ilmenite), a minimal sample preparation including sawing and rough polishing was performed to minimize specular reflection and increase the laser interaction with the target [28].

3. Results

CW and micro TR Raman spectra were collected at different positions within the LIBS craters and compared to spectra of pristine original materials, i.e. out of the LIBS crater. The LIBS craters were imaged by SEM for all samples. We first present results for all silicates, carbonates, phosphates and sulfates. Then, we present results obtained on oxides, sulfides and graphitic carbons with particular emphasis on the hematite target, which exhibits a phase transformation into magnetite within the LIBS crater. Here, one of the objectives is to detect potential transformations induced by the LIBS laser shots at the microscale and to see if they are detectable in the remote TR Raman mode. It is important to stress that LIBS craters measure about 400 micrometers in diameter, while the spot collected by the Raman remote setup at IMPMC is ≈6 mm in diameter. The Raman analytical footprint of SuperCam varies from 1.5 mm in diameter at a distance of 2 meters to 5.2 mm in diameter at a distance of 7 meters [10]. This means that the surface of LIBS craters is small compared to the area collected for Raman in both SuperCam and IMPMC configurations (around 7% in the worst case). On the other hand, the Mars 2020 deep UV Raman instrument (SHERLOC) has an analytical spot size (50 μm) smaller than the diameter of the LIBS craters and SHERLOC analyses could be affected by any laser-induced structural change in the LIBS craters. Similarly, if chemical modification happens in the LIBS crater, the PIXL analysis could be affected as well because the PIXL spot size is in the same range as the diameter of the LIBS craters.

3.1.Silicates, carbonates, phosphates and sulfates

Figure 1 shows representative SEM images of LIBS craters on silicates, carbonates, phosphates and sulfates (30 shots, Mars atmosphere). The depth, texture and microtexture of the craters are highly variable from one mineral to another (Figure 1). Noticeably, in the case of amethyst (Figure 1-a), microfractures in the crater are concoidal, which is typical of quartz, while there is a thin, apparently molten layer on top of the fractured surface for albite and oligoclase (Figure 1-b). For some samples like olivine, with surfaces ribbed by rough polishing prior to LIBS, craters appear shallow (Figure 1-c) with a rough floor showing a molten-like microtexture. Alternatively, in the case of andesine, the surface of the moderately deep crater is similar to the initial crystal surface not affected by LIBS (Figure 1-d), and the edges of the crater have a brittle-like microtexture with fractures following the cleavage pattern. Similar features are observed in the case of oligoclase (Figure 1-b). Some grains observed inside the crater were likely mechanically removed by the laser-target interaction or shockwave and then fell back into the crater.

The crater depths are different for powdered materials vs. hard samples (crystals, rocks). The depth of the LIBS craters for pellet samples (apatite FOH, apatite OH and gypsum 1) can reach several hundreds of micrometers up to a millimeter, while for the hard type samples, the depth extends to a few micrometers only [15,19,20]. In terms of microtexture, the crater in apatite OH has a molten appearance including bubble-shaped structures, while the crater of gypsum 1 does not exhibit any microtextural feature indicative of possible melting (Figure 1-e). The initial surface of hydromagnesite is covered by a secondary encrustation on top of the primary crystal (Figure 1-f). This surface crust is removed by the LIBS shots and the crater is shallow and affected by micro breaks with a conchoïdal aspect.

For all the silicates, carbonates, phosphates and sulfates analyzed by LIBS, regardless of the LIBS configuration, no mineralogical transformation was noticed based on CW and micro TR Raman spectroscopy. Figure 2 shows representative micro TR Raman spectra for some of these samples obtained on pristine areas far outside from the LIBS crater (in green) and inside the LIBS crater (in red). In all cases, Raman spectra measured inside *vs.* outside the craters exhibit the same peaks with no shift in wavenumber. However, variations in the relative intensities of several peaks are observed in some cases. For instance, in the case of olivine, Raman spectra exhibit the very same peaks corresponding to lattice vibrations (at 301 and 430 cm^{-1}) and internal modes (internal SiO_4 tetrahedral vibration at 822 and 855 cm^{-1}) inside

and outside the LIBS craters, with no significant variation in peak position or width (FWHM), but with an important intensity decrease. In the case of hydromagnesite, Raman spectra exhibit the same peaks corresponding to lattice vibrations (in the 100-400 cm^{-1} region) and internal modes (internal CO_3 stretching vibration at 1120 cm^{-1}) inside and outide the LIBS craters, with no significant variation in peak position and width (FWHM) but with an intensity decrease. The OH (≈3447 cm^{-1}) and H_2O (≈3516 cm^{-1}) bands are observed in the pristine crystal and are still present within the LIBS crater at the same wavenumber but with a relative intensity lower than that of the other modes observed at lower wavenumber, which may be indicative of slight dehydration.

While no change in the mineralogical structure is observed within the LIBS crater for these minerals, some changes are observed in the background intensity of the spectra. The ratio (R_{bkg}) of the background intensity of the micro TR Raman spectra collected inside LIBS craters over the background intensity of the spectra collected outside the crater was measured for all samples as described in the *Methodology - Raman spectroscopy* section (Table 2). The same intensity ratio was also calculated for the most intense Raman peak (R_{signal}) for all samples. Depending on the sample, the R_{signal} and R_{bkg} ratios are higher or lower than 1: for instance, R_{bkg} was lower than 1 in 7 cases over 13. In most cases (*e.g.* amethyst, hydromagnesite, olivine, gypsum 2), $R_{signal}<1$ which means that the relative intensity of the Raman signal inside the crater is lower than the one measured at the surface of the pristine sample. For andesine, hydroxyapatite and gypsum 1 however, the Raman signal is more intense within the LIBS crater ($R_{signal}>1$). The magnitude of such an intensity increase is very variable among samples: for instance, the background intensity of the FOH apatite increases by more than a factor of 6 ($R_{bkg}\approx6.7$), while that of hydroxyapatite increases by only 1.5x only ($R_{bkg}\approx1.5$) in craters. Similarly, while the peak intensity of amethyst is reduced by almost 8x ($R_{signal}\approx0.12$) in craters, that of gypsum 2 only drop by a factor of 1.33 ($R_{signal}\approx0.73$).

Figure 3-a and 3-b compare the remote TR Raman spectrum of pristine orthopyroxenite and hydromagnesite respectively (in green) and a spectrum with laser spot centered on a crater induced by 30 (in blue) and 100 (in red) LIBS shots. Besides slight differences in the background intensity, no structural and mineralogical modifications are visible in the Raman spectrum. More generally, for the other mineral phases described in this section, no significant difference in remote TR Raman spectra was observed between pristine areas and areas including a LIBS crater, regardless of the number of laser shots.

3.2. Fe-oxides, sulfides and graphitic carbon

Fe-oxides, sulfides and graphitic carbons are highly opaque and considerably absorb the incident laser light at infrared and visible wavelengths [4,29]. The surface of oxides and sulfides was made rough by sawing to minimize specular reflection and optimize LIBS laser coupling. SEM images (Figure 4) show that while the surface of pristine ilmenite is quite rough, the LIBS crater surface is shallow, smooth and has a molten appearance. Some thin cracks are observed at the crater surface, likely generated during thermal relaxation after the LIBS impact. The Raman spectrum of ilmenite shows a main peak at 680 cm^{-1}, corresponding to the symmetric stretching vibration of TiO_6 octahedra [30], plus other peaks between 200 and 500 cm^{-1} corresponding to lattice vibrations. Figure 5 shows a micro TR Raman spectrum obtained outside the crater and three Raman spectra obtained inside craters induced by 30 LIBS shots in an Earth atmosphere, in vacuum and in Martian atmosphere. Under all atmospheric conditions, the spectra collected inside the craters do not show any of the ilmenite peaks, but instead show two broad bands with low relative intensity, located at ≈137 and ≈721 cm^{-1}. The peak at 721 cm^{-1} may correspond to the former ilmenite peak at 680 cm^{-1} but is significantly broader and shifted towards higher wavenumbers, while attribution of the new broad band at ≈137 cm^{-1} remains enigmatic.

The LIBS crater in pyrite exhibits a molten metallic textural aspect (Figure 6). Figure 7-a shows a CW Raman map of a crater induced by 30 LIBS shots under Martian conditions. As observed by other studies [31], the pristine pyrite surface exhibits only 3 of the 5 Raman-active modes of pyrite likely due to polarization effects: at 343 cm^{-1} (vibrational mode, sulfur atoms displacement perpendicular to the S-S bond axis), at 378 cm^{-1} (in-phase stretching vibrations of the S_2 dumb-bells) and at 429 cm^{-1} (vibrationnal and stretching motions) [32]. Inside the crater, these peaks are significantly less intense and a new asymmetric peak at 451 cm^{-1} is observed. After LIBS shots, elemental sulfur is observed by Raman spectroscopy, with spectra exhibiting peaks at 153, 218 and 471 cm^{-1} (Figure 7-b, [33]); these were not observed on the initial pristine pyrite.

In hematite, LIBS-induced craters are shallow and exhibit a molten-like microtexture (Figure 8-a). CW Raman mapping reveals that the craters induced by 30 LIBS shots do not contain hematite anymore, but magnetite instead (Figure 9). Hematite exhibit bands at 291, 411, 500, 612 and 1322 cm^{-1}, while magnetite displays bands at 531 and 664 cm^{-1} [34]. A FIB thin foil (<100 nm in thicness) was extracted from inside the crater following the FIB lift-out method

(Figure 8-b). TEM imaging (Figure 8-c) and selected-area electron diffraction (SAED) were conducted on the FIB foil. The SAED pattern from the top molten layer of the FIB foil was consistent with magnetite viewed along the (112) zone axis with d_{-220} = 0.297 nm and $d_{11\text{-}1}$= 0.485 nm (Figure 8-d), confirming the presence of magnetite crystals with various orientations forming a continuous 200-nm-thick layer covering the surface of hematite within the LIBS crater. The thickness of this magnetite layer is nearly the same after 150 LIBS shots but is hardly visible in the 10 LIBS shots crater.

LIBS shots were performed on graphitic carbon samples only in a Martian atmosphere. The pristine coal is an immature low-rank coal, *i.e.* a disordered carbonaceous material as attested by the presence of large defect bands at ≈1200 and ≈1350 cm^{-1} (Figure 10-a). Such material is non crystalline and turbostratic, *i.e.* its aromatic skeleton contains complex chemical radicalization likely involving heteroatoms like H, O, N or S [24, 35]. In the LIBS crater, an intense background partly masking the Raman signal makes it difficult to conclude about the effect of LIBS on the structural organization of this coal. However, the presence of both large defect and graphite G bands means that the coal is neither fully amorphized, nor transformed into graphite. The pristine graphite is highly crystalline and exhibits a G band only (Figure 10-b). In the LIBS crater, different spectra are observed, indicating a wide variety of structures from quasi-amorphous (one broad band in the spectrum) to very disordered (one broad feature in which defect and G bands are detected) carbonaceous materials (Figure 10).

Remote TR Raman spectra of pristine hematite and pyrite, shown in figure 3-c and 3-d, are very similar to those centered on the LIBS craters (30 shots in blue and 100 shots in red), despite some slight differences in the background intensity.

4. Discussion

4.1. Pulsed-laser/sample interaction during LIBS and Raman analyses: thermal considerations

LIBS and Raman spectroscopy are both based on laser-sample interactions but rely on very different physical effects. LIBS probes the optical emission of a plasma generated by laser ablation of a target, while Raman probes the inelastic scattering of laser light within the sample. The LIBS laser pulse duration used here is 6 ns, so the interactions with the sample proceed through heating, melting and vaporization [36]. In contrast, laser-induced heating before or during Raman analyses should be minimal in order to avoid altering the spectra [37].

One of the most important parameters in laser-surface interaction is the optical penetration depth $\delta(\lambda)$, which is the distance over which the light is absorbed within the sample and its intensity reduced by 1/e. It is defined by:

$$\delta = \frac{1}{\alpha} = \frac{\lambda}{4\,\pi\,\kappa} \qquad \text{(equation 1)}$$

where α(λ) corresponds to the optical absorption coefficient of the sample of complex refractive index n(λ) + iκ(λ) at the laser wavelength λ. This optical absorption coefficient is high for opaque minerals (10^4 to 10^6 cm^{-1}) and much lower for translucent (10^2 to 10^4 cm^{-1}) and transparent (1 to 10^2 cm^{-1}) mineral phases. As an example, at a wavelength of 1064 nm, α(λ) is $4.8.10^5$ cm^{-1} for metallic iron [38] and close to 0 cm^{-1} for quartz [39]. These values yield an optical penetration depth $\delta(\lambda)$ of 20 nm for iron, while it amounts to meters for quartz, which is transparent at this wavelength. Therefore, the 1064 nm laser will penetrate into a quartz-like material much deeper than in an iron-like material. Consequently, the laser energy will be absorbed by a large volume within quartz, while it will be deposited within a thin layer at the sample surface and will trigger local heating in the case of iron-like material.

A second important parameter is the thermal penetration depth γ defined by:

$$\gamma = (D\tau)^{1/2} \qquad \text{(equation 2)}$$

where D corresponds to the thermal diffusivity and is defined by $D = k/\rho.C_p$, k being the thermal conductivity (see [40] for most minerals), ρ the density of the sample, C_p the specific heat and τ the laser pulse duration. The thermal penetration depth gives an idea about the propagation of heat from the heat source within the sample during the laser pulse: if γ is large, the local temperature increase induced by the laser absorption is low.

These two key parameters, δ(λ) and γ, provide a first-order insight into the temperature increase during a laser pulse for LIBS and Raman. We use the formalism for heating of solid targets by laser pulses provided by Bechtel (1975) [41]. To simplify his calculations, we assume (i) a fully homogeneous laser beam with a constant intensity (*i.e.* non gaussian) in both the time and space during the laser pulse and (ii) a thermal penetration depth γ that is negligible compared to the laser spot diameter (1D calculation). In addition, we assume no phase transition and do not consider latent heat of melting (corresponding to approximatively 10^{-2} mJ in the hematite case, well below our sensitivity). A possible effect of plasma shielding described by Bogaerts *et al.* [42] is not taken into account. Finally, temperature dependances of all thermodynamical properties have also been neglected. Using these hypotheses,

Bechtel's formalism allows us to calculate the temperature evolution as a function of depth *z* and time *t*:

For $0 \leq t \leq \tau$:

$$T(z,t) = A \cdot \left(f(z,t) + f(-z,t) + g(z,t) - exp^{\frac{-z}{\delta}} \right) \quad \text{(equation 3)}$$

For $t > \tau$:

$$T_{t>\tau}(z,t) = T(z,t) - T(z,t-\tau) \quad \text{(equation 4)}$$

with

$$f(z,t) = \frac{1}{2} exp^{\left(\frac{-z}{\delta}\right)} \cdot exp^{\left(\left(\frac{\gamma}{\delta}\right)^2 \cdot \frac{t}{\tau}\right)} \cdot erfc\left(\frac{\gamma}{\delta}\sqrt{\frac{t}{\tau}} - \frac{z}{2\gamma}\sqrt{\frac{\tau}{t}} \right)$$

$$g(z,t) = \frac{z}{2\sqrt{\pi}\delta} \boldsymbol{\Gamma}\left(\frac{-1}{2}, \left(\frac{z}{2\gamma}\right)^2 \cdot \frac{\tau}{t} \right)$$

$$A = \frac{(1-R) \cdot Irradiance}{\rho \cdot C_p} \cdot \left(\frac{\delta}{\gamma}\right)^2 \cdot \alpha \cdot \tau$$

where z (z > 0) is the depth from the sample surface, *t* the time elapsed after the laser hits the sample surface, and $R=((n-1)^2+\kappa^2)/((n+1)^2+\kappa^2)$ is the reflectivity of the sample ($n(\lambda)$ and $\kappa(\lambda)$ are the real and imaginary part of the refractive index) at the laser wavelength λ. *Irradiance* is the irradiance delivered at the sample surface during the shot, and erfc(x), Γ(a,x) are the error and incomplete gamma functions, respectively, other parameters being defined above.

To simplify the calculation, the experimental Gaussian pulse described in section 2.1 was transformed in a square pulsed shape in time and space. This was done by using correction factors ζ_t and ζ_ϕ ($\tau = \zeta_t \cdot \tau_{exp}$, $\phi = \zeta_\phi \cdot \phi_{exp}$, $\zeta_t = 1.413$ and $\zeta_\phi = 1.177$) assuming conservation of the pulse energy and its equi-repartition in both space and time.

Of course, such a calculation does not hold as soon as the sample is molten or undergoes phase transformation within the laser spot since the optical and thermodynamic properties of the sample change. In addition, most physical parameters relevant to characterize the target response are generally available for crystal samples that are ideal, which is not the case for most natural mineral phases such as those used in our experiments. However, the present theoretical approach provides an interesting first-order insight into the thermal aspects of the interactions of the pulsed laser with mineral targets.

4.2. No significant effects of LIBS laser shots on mineral structure for minerals with low optical absorption

Raman investigations do not reveal any phase transition induced by LIBS shots for the silicate-, carbonate-, phosphate- and sulfate-containing samples investigated here. For these transparent and translucent samples with very high $\delta(\lambda)$ values, the LIBS laser penetrates deep into the samples and the laser energy is released within a larger volume. Consequently, the temperature does not dramatically increase, and no mineralogical transformation occurs. In addition, because the Raman laser penetrates deep into these samples, the measured volume is large and potentially altered layers at the sample surface do not significantly contribute to the collected remote TR Raman signal.

Equation 4 predicts a low increase of temperature due to LIBS and Raman lasers at the surface of perfectly crystalline quartz, consistent with the absence of molten material in the craters induced by LIBS. The presence of molten material observed in craters induced by LIBS shots in olivine, orthopyroxenite and hydroxyapatite is consistent with their likely higher absorption coefficients at 1064 nm (exact values remain unknown).

The decrease of the background observed in Raman spectra collected within craters *vs.* outside craters for most transparent and translucent samples (6 out of 7) may be the consequence of a surface transformation of the sample inside the LIBS crater. LIBS ablation efficiency is affected not only by the sample roughness [43], but also by possible surface contamination like surface layers rich in water or hydroxyls [44] or deposits such as dirt or weathered layers [36]. These layers can interfere or even completely mask the analysis of the pristine material located beneath the surface by both LIBS and Raman spectroscopy. The repeated ablation during the LIBS laser burst removes these surface deposits [36]. In the case of ChemCam LIBS, data processing omits the first five LIBS spectra from the complete series of 30 LIBS shots to avoid contributions from these deposits [22]. The material within the crater is thus cleaner than the original surface of the sample, improving the quality of the Raman signal by reducing the background intensity. In addition to the effect of ablation within the LIBS crater, the plasma can also modify the surface over a large area. This has been seen, for exemple, with plasmas produced in an oxidizing environment, which then oxidize the surface surrounding the laser crater.

Powder pellet samples are aggregates of micrometer-sized crystalline grains that are discontiguous at the LIBS spot scale. The LIBS ablation is therefore highly effective, making

much deeper and steeper craters compared to single crystals or rocks: grains from the surface are efficiently removed by the laser energy and plasma expansion. Because of the removal of the grains from the surface, a fresh layer that is weakly- to non-impacted by the LIBS shots is exposed, exhibiting a Raman spectrum very similar to that of the pristine material. Note that some of the grains excavated during the LIBS shots fall down within and around the LIBS craters (*e.g.* Gypsum 1, Figure 1-e). Meanwhile, temperature may increase strongly at the surface of such powdered samples when impacted by the LIBS laser, with a temperature rise inversely proportional to the grain size [45]. The dissipation of energy is actually less efficient for such samples: phonons do not propagate at grain boundaries and air within the pores acts as a thermal insulator. The increase of the background observed for most of the pellet samples (4 out of 5) may be the consequence of a local laser-induced heating of the grains during the Raman analysis and/or light diffusion due to the randomly oriented grains deposit in the LIBS crater [45]. Much of the bedrock that are observed on Mars consists of relatively lightly cemented sandstones and mudstones [46]. Some of the effects observed on powder pellets in this study may therefore also apply to many of the observations on Mars.

4.3. Significant effects of LIBS laser shots on the structure for minerals with high optical absorption

The significant structural transformations of hematite, ilmenite, pyrite and graphitic carbons by LIBS shots are related to their high absorption coefficients at the LIBS laser wavelength. In the case of hematite, calculated temperature patterns versus depth and time are depicted on Figure 11.

The temperature rise at the hematite surface is high enough to reach a value in the range of the melting temperature of hematite (≈1838 K) and magnetite (≈1811 K) in 1 bar of air. The depth profile shows that the temperature is very high at the surface and exponentially decreases with depth. The time diagram shows that the temperature decrease is rapid and that the increase in temperature (few Kelvins) remaining 10 msec after the laser pulse is negligible. In other words, heat is nearly completely dissipated when the next LIBS laser pulse reaches the sample and there is no cumulative effect due to the repetition of laser pulses, as the rate of the laser is low enough (3Hz).

SEM observations reveal that the surface of the LIBS crater in hematite in Earth atmosphere is completely molten which means that the temperature of 1838 K at the surface of the hematite was actually reached and likely exceeded, in agreement with our theoretical

calculations. In a Mars atmosphere, the melting temperature of both hematite and magnetite can be estimated using the temperature-pressure diagram calculated for the Fe-O system by Ketteler *et al.* [47]. Assuming that the P_{O_2} corresponds to the maximum possible O_2 pressure achieved when all the CO_2 molecules of the martian atmosphere are broken into oxygen atoms in the LIBS plasma, the melting temperature is around 1680 K. SEM observations reveal that the surface of the LIBS crater in hematite in Mars atmosphere was completely molten as well (Figure 8-a) which implies that a temperature above 1680 K was reached at the sample surface during the LIBS analysis. These observations are in agreement with the temperature profiles retrieved from our theoretical calculations (Figure 11).

Notably, in both instances, quenching the melt leads to the crystallization of magnetite and not hematite as predicted by the temperature-pressure diagram calculated for the Fe-O system by Ketteler *et al.* [47]. This magnetite remains stable within the layer covering the LIBS crater and does not back-transform into hematite. The small thickness of the molten layer (about 200 nm as shown by TEM) is consistent with observations reported in the literature describing molten layer thicknesses below the micrometer for different materials and laser configurations [48,49]. The very fast cooling favors the crystallization of submicrometer-sized magnetite crystals. Interestingly, the depth at which the calculated temperature goes below the melting temperature of hematite (Figure 11-a) is slightly higher (because our 1D calculation underestimates the thermal losses), but within the same order of magnitude of the magnetite layer thickness as observed by TEM. Lastly, the thickness of the magnetite layer at the surface of hematite is large enough to explain why the Raman only probes magnetite and not the underlying hematite. Indeed, the high absorption coefficient α of magnetite at 532 nm [50], *i.e.* about 200 000 cm^{-1}, yields an optical penetration of ≈50 nm which is lower than the actual thickness observed for the magnetite layer.

Calculations of the temperature patterns with depth and time were also performed for pyrite and graphite. Because, these minerals have much higher absorption coefficients at 1064 nm compared to hematite, the temperature rise is significantly higher and can reach several thousands of Kelvins at the sample surface. In both cases, the time diagram shows that heat is completely released after 300 ms so that there is no cumulative effect from one pulse to another at 3 Hz. Such calculations were not feasible for ilmenite as we did not find a reliable value of the absorption coefficient for this mineral at 1064 nm.

In the case of ilmenite, the melting temperature is 1643 K at a pressure of 1 bar under Earth atmosphere. This temperature is likely reached as shown by the molten surface within the LIBS crater. A similar conclusion is reached in the case of LIBS shooting under a Mars atmosphere. In the LIBS crater, Raman spectra exhibit assymetrical, broad and weak bands supporting the presence of amorphous-like ilmenite. This suggests that during quenching the melt solidifies into an amorphous ilmenite-like phase rather than nanocrystalline ilmenite which has thinner and better defined Raman peaks [51,52].

The melting temperature of pyrite is 1450-1461 K at a pressure of 1 bar under Earth atmosphere. From theoretical calculations, this temperature is easily reached within the LIBS crater at the surface of the sample, in agreement with the molten aspect of the LIBS crater surface as observed by SEM. In the LIBS crater, pyrite apparently recrystallizes from the melt in a sligthly different configuration, as attested by the presence of a new peak at 451 cm^{-1}. This peak, absent from the pristine pyrite (Figure 7-b), may correspond to the combination of stretching and vibrational signal of four adjacent S_2 units [53] in the pyrite structure. At the temperature reached during the LIBS shots, some sulfur present in the melt is likely partially evaporated (boiling temperature of ≈700 K), forming elemental sulfur grains randomly distributed at the sample surface and observed by SEM and detected by Raman (Figure 7-a).

Lastly, the two graphitic carbons show a contrasting pattern. In the case of the coal sample, initially prepared as a powder pellet, LIBS excavation was efficient in the LIBS crater and removed the grains initially present at the surface, which were the most thermally affected by the LIBS shots sequence. In the crater, Raman spectra show an intense background which makes the identification of possible transformations difficult. In the case of graphite, Raman investigations show that the graphite structure was severely altered and locally amorphized in the LIBS crater generating an amorphous-like compound. This observation is in agreement with the molten aspect of graphite within the LIBS crater as observed by SEM and the temperature of several thousands of degrees achieved at the graphite surface as predicted by our theoretical calculations and likely higher than the melting temperature of graphite (between 3500 and 4450 K after [54]).

5. Concluding Remarks: Implications for combined LIBS-Raman analyses and Mars 2020 operations

A combination of LIBS and Raman spectroscopy in Earth or Material Sciences is increasingly popular as they provide complemetary information: chemical composition by LIBS, structure

by Raman. Our study shows that some caution has to be applied when combining these two methods at the microscale. First, the range of laser irradiances used for either CW or TR Raman spectroscopy are confirmed to be low enough to preserve the sample structure based on the data and the modeling. Normally, using Raman first before LIBS is probably the safest approach as the former is non-destructive. However, in some instances, using LIBS first is necessary to clean the surface of the sample or simply for operational reasons. The anticipated SuperCam strategy on Mars is to carry out LIBS first, followed by TR Raman, TR luminescence and/or IR analyses. This is mostly motivated by the need to remove an ubiquitous layer of dust covering the surface of Mars before further analysis [55,56]. Indeed, if not removed, dust would clearly complicate or prevent TR Raman/TR luminescence analyses by absorbing the incident laser light. However, this dust can be partially removed by shooting few laser pulses as shown by MSL ChemCam operations [15,57,58] detected.

Our study shows that LIBS laser shots have minimal impact for minerals having low optical absorption coefficients at 1064 nm like silicates, carbonates, phosphates and sulfates. In this case, only variations in the relative intensities of the Raman peaks and background are noticed and the main structural information is preserved. In the case of materials such as Fe-Ti-oxides, sulfides and graphitic carbons which absorb strongly at 1064 nm, LIBS can cause melting, phase transformation and/or amorphization within the crater which may affect the Raman signature. Since remote Raman analyses in SuperCam configuration probe a significantly larger surface than that impacted by LIBS shots, possible alteration of Raman signatures in the LIBS crater should not be visible in the Raman spectra collected by SuperCam, even in the case of highly absorbing minerals.

Proximity instruments SHERLOC and/or PIXL may be used in the area affected by prior LIBS analysis for instance to take advantage of the dust-free area, to investigate the effects of LIBS laser shots or for cross-analysis between instruments. The PIXL elemental cross-comparison with SuperCam-LIBS would actually need to be within the crater itself, while the SHERLOC cross-comparison with SuperCam-Raman would only need to be in the millimeter or two dust-free area around the crater if the arm positioning is precise enough. In these cases, it will be important to assess if LIBS-induced damages could affect their analysis, as they will work at higher spatial resolution typically in the range of the LIBS laser spots. This is especially important for highly absorbing targets at 1064 nm that could be damaged by LIBS laser shots.

Acknowledgements

This research was part of a PhD thesis supported by Labex Matisse. Funding of this research by Sorbonne Université and CNRS INP is acknowledged. The NASA Mars Exploration Program supported some parts (ChemCam body unit), and LIBS experiments were conducted at Institut de Recherche en Astrophysique et Planétologie (IRAP) with support from CNES. This research was conducted in the frame of the Mars 2020 mission and SuperCam instrument.

References:

[1] I. Osticioli, N.F.C. Mendes, A. Nevin, F.P.S.C. Gil, M. Becucci, E. Castellucci, Analysis of natural and artificial ultramarine blue pigments using laser induced breakdown and pulsed Raman spectroscopy, statistical analysis and light microscopy, Spectrochim Acta A Mol Biomol Spectrosc. 73 (2009) 525–531. doi:10.1016/j.saa.2008.11.028.

[2] Y. Maruyama, J. Blacksberg, E. Charbon, A 1024 x 8, 700-ps Time-Gated SPAD Line Sensor for Planetary Surface Exploration With Laser Raman Spectroscopy and LIBS, IEEE Journal of Solid-State Circuits. 49 (2014) 179–189. doi:10.1109/JSSC.2013.2282091.

[3] R.C. Wiens, S.K. Sharma, J. Thompson, A. Misra, P.G. Lucey, Joint analyses by laser-induced breakdown spectroscopy (LIBS) and Raman spectroscopy at stand-off distances, Spectrochim Acta A Mol Biomol Spectrosc. 61 (2005) 2324–2334. doi:10.1016/j.saa.2005.02.031.

[4] S.K. Sharma, A.K. Misra, P.G. Lucey, R.C.F. Lentz, A combined remote Raman and LIBS instrument for characterizing minerals with 532nm laser excitation, Spectrochimica Acta Part A: Molecular and Biomolecular Spectroscopy. 73 (2009) 468–476. doi:10.1016/j.saa.2008.08.005.

[5] S.M. Clegg, R. Wiens, A.K. Misra, S.K. Sharma, J. Lambert, S. Bender, R. Newell, K. Nowak-Lovato, S. Smrekar, M.D. Dyar, S. Maurice, Planetary geochemical investigations using Raman and laser-induced breakdown spectroscopy, Appl Spectrosc. 68 (2014) 925–936. doi:10.1366/13-07386.

[6] S.-J. Choi, J.-J. Choi, J.J. Yoh, Advancing the experimental design for simultaneous acquisition of laser induced plasma and Raman signals using a single pulse, Spectrochimica Acta Part B: Atomic Spectroscopy. 123 (2016) 1–5. doi:10.1016/j.sab.2016.07.006.

[7] J. Moros, M.M. ElFaham, J.J. Laserna, Dual-Spectroscopy Platform for the Surveillance of Mars Mineralogy Using a Decisions Fusion Architecture on Simultaneous LIBS-Raman Data, Anal. Chem. 90 (2018) 2079–2087. doi:10.1021/acs.analchem.7b04124.

[8] A.K. Misra, T.E. Acosta-Maeda, J.N. Porter, G. Berlanga, D. Muchow, S.K. Sharma, B. Chee, A Two Components Approach for Long Range Remote Raman and Laser-Induced Breakdown (LIBS) Spectroscopy Using Low Laser Pulse Energy, Appl. Spectrosc., AS. 73 (2019) 320–328. doi:10.1177/0003702818812144.

[2] mars.nasa.gov, « Science - Mars 2020 Rover ». http://mars.nasa.gov/mars2020/mission/science/ (accessed July 15, 2019).

[10] R.C. Wiens, S. Maurice, F. Rull Perez, The SuperCam Remote Sensing Instrument Suite for the Mars 2020 Rover: A Preview, Spectroscopy 32(5), 50-55 (2017). http://www.spectroscopyonline.com/supercam-remote-sensing-instrument-suite-mars-2020-rover-preview (accessed July 15, 2019)

[11] S. Maurice, R.C. Wiens, M. Saccoccio, B. Barraclough, O. Gasnault, O. Forni, N. Mangold, D. Baratoux, S. Bender, G. Berger, J. Bernardin, M. Berthé, N. Bridges, D. Blaney, M. Bouyé, P. Caïs, B. Clark, S. Clegg, A. Cousin, D. Cremers, A. Cros, L. DeFlores, C. Derycke, B. Dingler, G. Dromart, B. Dubois, M. Dupieux, E. Durand, L. d'Uston, C. Fabre, B. Faure, A. Gaboriaud, T. Gharsa, K. Herkenhoff, E. Kan, L. Kirkland, D. Kouach, J.-L. Lacour, Y. Langevin, J. Lasue, S.L. Mouélic, M. Lescure, E. Lewin, D. Limonadi, G. Manhès, P. Mauchien, C. McKay, P.-Y. Meslin, Y. Michel, E. Miller, H.E. Newsom, G. Orttner, A. Paillet, L. Parès, Y. Parot, R. Pérez, P. Pinet, F. Poitrasson, B. Quertier, B. Sallé, C. Sotin, V. Sautter, H. Séran, J.J. Simmonds, J.-B. Sirven, R. Stiglich, N. Striebig, J.-J. Thocaven, M.J. Toplis, D. Vaniman, The ChemCam Instrument Suite on the Mars Science Laboratory (MSL) Rover: Science Objectives and

Mast Unit Description, Space Sci Rev. 170 (2012) 95–166. doi:10.1007/s11214-012-9912-2.

[12] R.C. Wiens, S. Maurice, B. Barraclough, M. Saccoccio, W.C. Barkley, J.F. Bell, S. Bender, J. Bernardin, D. Blaney, J. Blank, M. Bouyé, N. Bridges, N. Bultman, P. Caïs, R.C. Clanton, B. Clark, S. Clegg, A. Cousin, D. Cremers, A. Cros, L. DeFlores, D. Delapp, R. Dingler, C. D'Uston, M. Darby Dyar, T. Elliott, D. Enemark, C. Fabre, M. Flores, O. Forni, O. Gasnault, T. Hale, C. Hays, K. Herkenhoff, E. Kan, L. Kirkland, D. Kouach, D. Landis, Y. Langevin, N. Lanza, F. LaRocca, J. Lasue, J. Latino, D. Limonadi, C. Lindensmith, C. Little, N. Mangold, G. Manhes, P. Mauchien, C. McKay, E. Miller, J. Mooney, R.V. Morris, L. Morrison, T. Nelson, H. Newsom, A. Ollila, M. Ott, L. Pares, R. Perez, F. Poitrasson, C. Provost, J.W. Reiter, T. Roberts, F. Romero, V. Sautter, S. Salazar, J.J. Simmonds, R. Stiglich, S. Storms, N. Striebig, J.-J. Thocaven, T. Trujillo, M. Ulibarri, D. Vaniman, N. Warner, R. Waterbury, R. Whitaker, J. Witt, B. Wong-Swanson, The ChemCam Instrument Suite on the Mars Science Laboratory (MSL) Rover: Body Unit and Combined System Tests, Space Sci Rev. 170 (2012) 167–227. doi:10.1007/s11214-012-9902-4.

[13] P.-Y. Meslin, O. Gasnault, O. Forni, S. Schröder, A. Cousin, G. Berger, S.M. Clegg, J. Lasue, S. Maurice, V. Sautter, S.L. Mouélic, R.C. Wiens, C. Fabre, W. Goetz, D. Bish, N. Mangold, B. Ehlmann, N. Lanza, A.-M. Harri, R. Anderson, E. Rampe, T.H. McConnochie, P. Pinet, D. Blaney, R. Léveillé, D. Archer, B. Barraclough, S. Bender, D. Blake, J.G. Blank, N. Bridges, B.C. Clark, L. DeFlores, D. Delapp, G. Dromart, M.D. Dyar, M. Fisk, B. Gondet, J. Grotzinger, K. Herkenhoff, J. Johnson, J.-L. Lacour, Y. Langevin, L. Leshin, E. Lewin, M.B. Madsen, N. Melikechi, A. Mezzacappa, M.A. Mischna, J.E. Moores, H. Newsom, A. Ollila, R. Perez, N. Renno, J.-B. Sirven, R. Tokar, M. de la Torre, L. d'Uston, D. Vaniman, A. Yingst, M.S. Team, Soil Diversity and Hydration as Observed by ChemCam at Gale Crater, Mars, Science. 341 (2013) 1238670. doi:10.1126/science.1238670.

[14] R.C. Wiens, S. Maurice, the ChemCam and MSL Science Teams, ChemCam: Chemostratigraphy by the first Mars microprobe, Elements 11, 33-38. (2015). doi:10.2113/gselements.11.1.33.

[15] S. Maurice, S.M. Clegg, R.C. Wiens, O. Gasnault, W. Rapin, O. Forni, A. Cousin, V. Sautter, N. Mangold, L.L. Deit, M. Nachon, R.B. Anderson, N.L. Lanza, C. Fabre, V. Payré, J. Lasue, P.-Y. Meslin, R.J. Léveillé, B.L. Barraclough, P. Beck, S.C. Bender, G. Berger, J.C. Bridges, N.T. Bridges, G. Dromart, M.D. Dyar, R. Francis, J. Frydenvang, B. Gondet, B.L. Ehlmann, K.E. Herkenhoff, J.R. Johnson, Y. Langevin, M.B. Madsen, N. Melikechi, J.-L. Lacour, S.L. Mouélic, E. Lewin, H.E. Newsom, A.M. Ollila, P. Pinet, S. Schröder, J.-B. Sirven, R.L. Tokar, M.J. Toplis, C. d'Uston, D.T. Vaniman, A.R. Vasavada, ChemCam activities and discoveries during the nominal mission of the Mars Science Laboratory in Gale crater, Mars, J. Anal. At. Spectrom. 31 (2016) 863–889. doi:10.1039/C5JA00417A.

[16] T. Fouchet, F. Montmessin, O. Forni, S. Maurice, R.C. Wiens, J.R. Johnson, S.M. Clegg, P. Beck, F. Poulet, O. Gasnault, P.-Y. Meslin, the SuperCam team, The infrared investigation on the SuperCam instrument for the Mars 2020 rover., Lunar Planet. Sci. XLVI, 1736, The Lunar and Planetary Institute, Houston, TX. (2015). http://adsabs.harvard.edu/abs/2015LPI....46.1736F (accessed July 15, 2019).

[17] N. Murdoch, B. Chide, J. Lasue, A. Cadu, A. Sournac, M. Bassas-Portús, X. Jacob, J. Merrison, J.J. Iversen, C. Moretto, C. Velasco, L. Parès, A. Hynes, V. Godiver, R.D. Lorenz, P. Cais, P. Bernadi, S. Maurice, R.C. Wiens, D. Mimoun, Laser-induced breakdown spectroscopy acoustic testing of the Mars 2020 microphone, Planetary and Space Science. 165 (2019) 260–271. doi:10.1016/j.pss.2018.09.009.

[18] O. Gasnault, S. Maurice, R.C. Wiens, S. Le Mouélic, W.W. Fischer, P. Caïs, K. McCabe, J.-M. Reess, C. Virmontois, SuperCam Remote Micro-Imager on Mars 2020, in: 2015: p. 2990. http://adsabs.harvard.edu/abs/2015LPI....46.2990G (accessed July 15, 2019).
[19] S. Maurice, A. Cousin, R.C. Wiens, O. Gasnault, L. Parès, O. Forni, P.-Y. Meslin, S. Clegg, Chemcam Team, Laser Induced Breakdown Spectroscopy (LIBS) Spot Size at Stand-Off Distances with ChemCam, in: 2012: p. 2899. http://adsabs.harvard.edu/abs/2012LPI....43.2899M (accessed July 15, 2019).
[20] B. Chide, S. Maurice, N. Murdoch, J. Lasue, B. Bousquet, X. Jacob, A. Cousin, O. Forni, O. Gasnault, P.-Y. Meslin, J.-F. Fronton, M. Bassas-Portús, A. Cadu, A. Sournac, D. Mimoun, R.C. Wiens, Listening to laser sparks: a link between Laser-Induced Breakdown Spectroscopy, acoustic measurements and crater morphology, Spectrochimica Acta Part B: Atomic Spectroscopy. 153 (2019) 50–60. doi:10.1016/j.sab.2019.01.008.
[21] A. Cousin, O. Forni, S. Maurice, O. Gasnault, C. Fabre, V. Sautter, R.C. Wiens, J. Mazoyer, Laser induced breakdown spectroscopy library for the Martian environment, Spectrochimica Acta Part B: Atomic Spectroscopy. 66 (2011) 805–814. doi:10.1016/j.sab.2011.10.004.
[22] W. Rapin, P.-Y. Meslin, S. Maurice, R.C. Wiens, D. Laporte, B. Chauviré, O. Gasnault, S. Schröder, P. Beck, S. Bender, O. Beyssac, A. Cousin, E. Dehouck, C. Drouet, O. Forni, M. Nachon, N. Melikechi, B. Rondeau, N. Mangold, N.H. Thomas, Quantification of water content by laser induced breakdown spectroscopy on Mars, Spectrochimica Acta Part B: Atomic Spectroscopy. 130 (2017) 82–100. doi:10.1016/j.sab.2017.02.007.
[23] S. Bernard, O. Beyssac, K. Benzerara, Raman Mapping Using Advanced Line-Scanning Systems: Geological Applications, Appl. Spectrosc., AS. 62 (2008) 1180–1188. doi:10.1366/000370208786401581.
[24] O. Beyssac, M. Gauthier, A. Fau, S. Bernard, K. Benzerara, M. Morand, P. Rosier, P.-Y. Meslin, S. Maurice, SuperCam Science Team, Nanosecond Time-Resolved Raman and Fluorescence Spectroscopy: Insights for Mineral and Organics Characterization, in: 2017: p. 1545. http://adsabs.harvard.edu/abs/2017LPI....48.1545B (accessed July 15, 2019).
[25] S. Bernard, K. Benzerara, O. Beyssac, G.E. Brown, Multiscale characterization of pyritized plant tissues in blueschist facies metamorphic rocks, Geochimica et Cosmochimica Acta. 74 (2010) 5054–5068. doi:10.1016/j.gca.2010.06.011.
[26] K. Benzerara, N. Menguy, M. Obst, J. Stolarski, M. Mazur, T. Tylisczak, G.E. Brown, A. Meibom, Study of the crystallographic architecture of corals at the nanoscale by scanning transmission X-ray microscopy and transmission electron microscopy, Ultramicroscopy. 111 (2011) 1268–1275. doi:10.1016/j.ultramic.2011.03.023.
[27] S.M. Hosseini, C. Drouet, A. Al-Kattan, A. Navrotsky, Energetics of lanthanide-doped calcium phosphate apatite, American Mineralogist. 99 (2014) 2320–2327. doi:10.2138/am-2014-4930.
[28] C. López-Moreno, S. Palanco, J. J. Laserna, Remote laser-induced plasma spectrometry for elemental analysis of samples of environmental interest, Journal of Analytical Atomic Spectrometry. 19 (2004) 1479–1484. doi:10.1039/B408534E.
[29] O. Beyssac, M. Lazzeri, Application of Raman spectroscopy to the study of graphitic carbons in the Earth Sciences, in: J. Dubessy, M.C. Caumon, F. Rull (Eds.), Applications of Raman Spectroscopy to Earth Sciences and Cultural Heritage, Mineralogical Society Great Britain & Ireland, London, 2012: pp. 415–454. https://www.minersoc.org/EMU-notes-12-12.html (accessed July 15, 2019).

[30] A. Wang, K.E. Kuebler, B.L. Jolliff, L.A. Haskin, Raman spectroscopy of Fe-Ti-Cr-oxides, case study: Martian meteorite EETA79001, American Mineralogist. 89 (2004) 665–680. doi:10.2138/am-2004-5-601.
[31] A.K. Kleppe, A.P. Jephcoat, High-pressure Raman spectroscopic studies of FeS2 pyrite, Mineralogical Magazine. 68 (2004) 433–441. doi:10.1180/0026461046830196.
[32] C. Sourisseau, R. Cavagnat, M. Fouassier, The vibrational properties and valence force fields of FeS2, RuS2 pyrites and FeS2 marcasite, Journal of Physics and Chemistry of Solids. 52 (1991) 537–544. doi:10.1016/0022-3697(91)90188-6.
[33] B.A. Trofimov, L.M. Sinegovskaya, N.K. Gusarova, Vibrations of the S–S bond in elemental sulfur and organic polysulfides: a structural guide, Journal of Sulfur Chemistry. 30 (2009) 518–554. doi:10.1080/17415990902998579.
[34] S.J. Oh, D.C. Cook, H.E. Townsend, Characterization of Iron Oxides Commonly Formed as Corrosion Products on Steel, Hyperfine Interactions. 112 (1998) 59–66. doi:10.1023/A:1011076308501.
[35] P.R. Buseck, O. Beyssac, From organic matter to graphite: Graphitization, ELEMENTS. 10 (2014) 421–426. doi:10.2113/gselements.10.6.421.
[36] D.A. Cremers, L.J. Radziemski, Handbook of Laser-Induced Breakdown Spectroscopy: Cremers/Handbook of Laser-induced Breakdown Spectroscopy, John Wiley & Sons, Ltd, Chichester, UK, 2006. doi:10.1002/0470093013.
[37] L. Nasdala, D.C. Smith, R. Kaindl, M.A. Ziemann, Raman spectroscopy: Analytical perspectives in mineralogical research, in: G. Papp, T.G. Weiszburg, A. Beran, E. Libowitzky (Eds.), Spectroscopic Methods in Mineralogy, Mineralogical Society of Great Britain and Ireland, Germany, 2004: pp. 281–343. doi:10.1180/EMU-notes.6.7.
[38] P.B. Johnson, R.W. Christy, Optical constants of transition metals: Ti, V, Cr, Mn, Fe, Co, Ni, and Pd, Phys. Rev. B. 9 (1974) 5056–5070. doi:10.1103/PhysRevB.9.5056.
[39] G. Ghosh, Dispersion-equation coefficients for the refractive index and birefringence of calcite and quartz crystals, Optics Communications. 163 (1999) 95–102. doi:10.1016/S0030-4018(99)00091-7.
[40] K. Horai, G. Simmons, Thermal conductivity of rock-forming minerals, Earth and Planetary Science Letters. 6 (1969) 359–368. doi:10.1016/0012-821X(69)90186-1.
[41] J.H. Bechtel, Heating of solid targets with laser pulses, Journal of Applied Physics. 46 (1975) 1585–1593. doi:10.1063/1.321760.
[42] A. Bogaerts, Z. Chen, R. Gijbels, A. Vertes, Laser ablation for analytical sampling: what can we learn from modeling?, Spectrochimica Acta Part B: Atomic Spectroscopy. 58 (2003) 1867–1893. doi:10.1016/j.sab.2003.08.004.
[43] I. Lopez-Quintas, V. Piñon, M.P. Mateo, G. Nicolas, Effect of surface topography in the generation of chemical maps by laser-induced plasma spectroscopy, Applied Surface Science. 258 (2012) 9432–9436. doi:10.1016/j.apsusc.2012.04.026.
[44] K.H. Kurniawan, M.O. Tjia, K. Kagawa, Review of Laser-Induced Plasma, Its Mechanism, and Application to Quantitative Analysis of Hydrogen and Deuterium, Applied Spectroscopy Reviews. 49 (2014) 323–434. doi:10.1080/05704928.2013.825267.
[45] F. Foucher, G. Lopes-Reyes, N. Bost, F. Rull-Perez, P. Rüβmann, F. Westall, Effect of grain size distribution on Raman analyses and the consequences for in situ planetary missions, Journal of Raman Spectroscopy. 44 (2013) 916–925. doi:10.1002/jrs.4307.
[46] R.E. Arvidson, P. Bellutta, F. Calef, A.A. Fraeman, J.B. Garvin, O. Gasnault, J.A. Grant, J.P. Grotzinger, V.E. Hamilton, M. Heverly, K.A. Iagnemma, J.R. Johnson, N. Lanza, S. Le Mouélic, N. Mangold, D.W. Ming, M. Mehta, R.V. Morris, H.E. Newsom, N. Rennó, D. Rubin, J. Schieber, R. Sletten, N.T. Stein, F. Thuillier, A.R. Vasavada, J. Vizcaino, R.C. Wiens, Terrain physical properties derived from orbital data and the first 360 sols

of Mars Science Laboratory Curiosity rover observations in Gale Crater, Journal of Geophysical Research: Planets. 119 (2014) 1322–1344. doi:10.1002/2013JE004605.
[47] G. Ketteler, W. Weiss, W. Ranke, R. Schlögl, Bulk and surface phases of iron oxides in an oxygen and water atmosphere at low pressure, Phys. Chem. Chem. Phys. 3 (2001) 1114–1122. doi:10.1039/B009288F.
[48] J. Cole, P. Humphreys, L. Earwaker, A melting model for pulsed laser heating of silicon, Vacuum. 34 (1984) 871–874. doi:10.1016/0042-207X(84)90166-0.
[49] D. Sands, Pulsed Laser Heating and Melting, Heat Transfer - Engineering Applications. (2011). doi:10.5772/28736.
[50] A. Schlegel, S.F. Alvarado, P. Wachter, Optical properties of magnetite (Fe3O4), Journal of Physics C Solid State Physics. 12 (1979) 1157–1164. doi:10.1088/0022-3719/12/6/027.
[51] A.T. Raghavender, N.H. Hong, K.J. Lee, M.-H. Jung, Z. Skoko, M. Vasilevskiy, M.F. Cerqueira, A.P. Samantilleke, Nano-ilmenite FeTiO3: Synthesis and characterization, J Mag Mag Mater. 331 (2013) 129–132. doi:10.1016/j.jmmm.2012.11.028.
[52] D. Tuschel, Why Are the Raman Spectra of Crystalline and Amorphous Solids Different?, http://www.spectroscopyonline.com/why-are-raman-spectra-crystalline-and-amorphous-solids-different (accessed July 15, 2019).
[53] M. Khabbaz, M.H. Entezari, Simple and versatile one-step synthesis of FeS2 nanoparticles by ultrasonic irradiation, J Colloid Interface Sci. 470 (2016) 204–210. doi:10.1016/j.jcis.2016.02.055.
[54] A.I. Savvatimskiy, Measurements of the melting point of graphite and the properties of liquid carbon (a review for 1963–2003), Carbon. 43 (2005) 1115–1142. doi:10.1016/j.carbon.2004.12.027.
[55] C. Sagan, J.B. Pollack, Windblown Dust on Mars, Nature. 223 (1969) 791–794. doi:10.1038/223791a0.
[56] P.R. Christensen, Regional dust deposits on Mars: Physical properties, age, and history, Journal of Geophysical Research: Solid Earth. 91 (1986) 3533–3545. doi:10.1029/JB091iB03p03533.
[57] T.G.M. Graff, Dust Removal on Mars Using Laser-Induced Breakdown Spectroscopy, , Lunar Planet. Sci. XLII, The Lunar and Planetary Institute, Houston, TX. (2011). https://ntrs.nasa.gov/search.jsp?R=20110007830 (accessed July 15, 2019).
[58] J. Lasue, N. Mangold, A. Cousin, P.-Y. Meslin, R. Wiens, O. Gasnault, W. Rapin, S. Schroder, A. Ollila, C. Fabre, G. Berger, S. Le Mouélic, E. Dehouck, O. Forni, S. Maurice, R. Anderson, N. Bridges, B. Clark, S. Clegg, C. d'Uston, W. Goetz, J.R. Johnson, N. Lanza, M. Madsen, N. Melikechi, H. Newsom, V. Sautter, J. Martin-Torres, M.-P. Zorzano, MSL Science Team, ChemCam analysis of Martian fine dust, in: 2016: p. 507.06. http://adsabs.harvard.edu/abs/2016DPS....4850706L (accessed July 15, 2019).
[59] E.B. Rampe, D.W. Ming, D.F. Blake, T.F. Bristow, S.J. Chipera, J.P. Grotzinger, R.V. Morris, S.M. Morrison, D.T. Vaniman, A.S. Yen, C.N. Achilles, P.I. Craig, D.J. Des Marais, R.T. Downs, J.D. Farmer, K.V. Fendrich, R. Gellert, R.M. Hazen, L.C. Kah, J.M. Morookian, T.S. Peretyazhko, P. Sarrazin, A.H. Treiman, J.A. Berger, J. Eigenbrode, A.G. Fairén, O. Forni, S. Gupta, J.A. Hurowitz, N.L. Lanza, M.E. Schmidt, K. Siebach, B. Sutter, L.M. Thompson, Mineralogy of an ancient lacustrine mudstone succession from the Murray formation, Gale crater, Mars, Earth and Planetary Science Letters. 471 (2017) 172–185. doi:10.1016/j.epsl.2017.04.021.
[60] A. Cousin, V. Sautter, V. Payré, O. Forni, N. Mangold, O. Gasnault, L. Le Deit, J. Johnson, S. Maurice, M. Salvatore, R.C. Wiens, P. Gasda, W. Rapin, Classification of igneous rocks analyzed by ChemCam at Gale crater, Mars, Icarus. 288 (2017) 265–283. doi:10.1016/j.icarus.2017.01.014.

[61] H.Y. McSween, R.E. Arvidson, J.F. Bell, D. Blaney, N.A. Cabrol, P.R. Christensen, B.C. Clark, J.A. Crisp, L.S. Crumpler, D.J.D. Marias, J.D. Farmer, R. Gellert, A. Ghosh, S. Gorevan, T. Graff, J. Grant, L.A. Haskin, K.E. Herkenhoff, J.R. Johnson, B.L. Jolliff, G. Klingelhoefer, A.T. Knudson, S. McLennan, K.A. Milam, J.E. Moersch, R.V. Morris, R. Rieder, S.W. Ruff, P.A.D. Souza, S.W. Squyres, H. Wänke, A. Wang, M.B. Wyatt, A. Yen, J. Zipfel, Basaltic rocks analyzed by the Spirit rover in Gusev crater, Sciece, Sciecne, SCIENCE, Science (New York, N.Y.), Science Science, Science,, Science., Sciencee, SCIENCES. 305 (2004) 842–845. doi:10.1126/science.1099851.

[62] D.L. Bish, D.F. Blake, D.T. Vaniman, S.J. Chipera, R.V. Morris, D.W. Ming, A.H. Treiman, P. Sarrazin, S.M. Morrison, R.T. Downs, C.N. Achilles, A.S. Yen, T.F. Bristow, J.A. Crisp, J.M. Morookian, J.D. Farmer, E.B. Rampe, E.M. Stolper, N. Spanovich, M.S. Team, X-ray Diffraction Results from Mars Science Laboratory: Mineralogy of Rocknest at Gale Crater, Science. 341 (2013) 1238932. doi:10.1126/science.1238932.

[63] A.H. Treiman, G.A. McKay, D.D. Bogard, D.W. Mittlefehldt, M.-S. Wang, L. Keller, M.E. Lipschutz, M.M. Lindstrom, D. Garrison, Comparison of the LEW88516 and ALHA77005 martian meteorites: Similar but distinct, Meteoritics. 29 (1994) 581–592. doi:10.1111/j.1945-5100.1994.tb00771.x.

[64] D.W. Mittlefehldt, ALH84001, a cumulate orthopyroxenite member of the martian meteorite clan, Meteoritics. 29 (1994) 214–221. doi:10.1111/j.1945-5100.1994.tb00673.x.

[65] C.B. Agee, N.V. Wilson, F.M. McCubbin, K. Ziegler, V.J. Polyak, Z.D. Sharp, Y. Asmerom, M.H. Nunn, R. Shaheen, M.H. Thiemens, A. Steele, M.L. Fogel, R. Bowden, M. Glamoclija, Z. Zhang, S.M. Elardo, Unique Meteorite from Early Amazonian Mars: Water-Rich Basaltic Breccia Northwest Africa 7034, Science. 339 (2013) 780–785. doi:10.1126/science.1228858.

[66] P.B. Niles, D.C. Catling, G. Berger, E. Chassefière, B.L. Ehlmann, J.R. Michalski, R. Morris, S.W. Ruff, B. Sutter, Geochemistry of Carbonates on Mars: Implications for Climate History and Nature of Aqueous Environments, Space Sci Rev. 174 (2013) 301–328. doi:10.1007/s11214-012-9940-y.

[67] O. Forni, M. Gaft, M.J. Toplis, S.M. Clegg, S. Maurice, R.C. Wiens, N. Mangold, O. Gasnault, V. Sautter, S. Le Mouélic, P.-Y. Meslin, M. Nachon, R.E. McInroy, A.M. Ollila, A. Cousin, J.C. Bridges, N.L. Lanza, M.D. Dyar, First detection of fluorine on Mars: Implications for Gale Crater's geochemistry, Geophys. Res. Lett. 42 (2015) 2014GL062742. doi:10.1002/2014GL062742.

[68] A. Gendrin, N. Mangold, J.-P. Bibring, Y. Langevin, B. Gondet, F. Poulet, G. Bonello, C. Quantin, J. Mustard, R. Arvidson, S. LeMouélic, Sulfates in Martian Layered Terrains: The OMEGA/Mars Express View, Science. 307 (2005) 1587–1591. doi:10.1126/science.1109087.

[69] D.T. Vaniman, G.M. Martínez, E.B. Rampe, T.F. Bristow, D.F. Blake, A.S. Yen, D.W. Ming, W. Rapin, P.Y. Meslin, J.M. Morookian, R.T. Downs, S.J. Chipera, R.V. Morris, S.M. Morrison, A.H. Treiman, C.N. Achilles, K. Robertson, J.P. Grotzinger, R.M. Hazen, R.C. Wiens, D.Y. Sumner, Gypsum, bassanite, and anhydrite at Gale crater, Mars, American Mineralogist. 103 (2018) 1011–1020. doi:10.2138/am-2018-6346.

[70] A. Steele, F.M. McCubbin, M.D. Fries, The provenance, formation, and implications of reduced carbon phases in Martian meteorites, Meteoritics & Planetary Science. (2016). doi:10.1111/maps.12670.

[71] C.K. Shearer, G.D. Layne, J.J. Papike, M.N. Spilde, Sulfur isotopic systematics in alteration assemblages in martian meteorite Allan Hills 84001, Geochimica et Cosmochimica Acta. 60 (1996) 2921–2926. doi:10.1016/0016-7037(96)00165-2.

[72] J.P. Greenwood, L.R. Riciputi, H.Y. McSween, Sulfide isotopic compositions in shergottites and ALH84001, and possible implications for life on Mars, Geochimica et Cosmochimica Acta. 61 (1997) 4449–4453. doi:10.1016/S0016-7037(97)00246-9.
[73] P.R. Christensen, J.L. Bandfield, R.N. Clark, K.S. Edgett, Detection of crystalline hematite mineralization on Mars by the Thermal Emission Spectrometer: Evidence for near-surface water - 2000 - Journal of Geophysical Research: Planets Vol.105 No E4 (2000) 9623-9642. doi:10.1029/1999JE001093.

Figure captions:

Figure 1: SEM images of some representative LIBS craters for silicates, carbonates, phosphates and sulfates minerals obtained in backscattered electrons mode. Samples represented are: (a) amethyst, (b) oligoclase, (c) olivine, (d) andesine, (e) gypsum 1, (f) hydromagnesite. For each example, the large image (left) depicts the whole crater, the top small image on the right side depicts the sample surface within the LIBS crater and the bottom small image on the right side depicts the pristine sample surface out of the crater. Scale bars indicate 100 µm for each large image and 40 µm for each small image. The 90 µm laser spot diameter for micro time-resolved Raman spectroscopy is sketched in green.

Figure 2: Micro Time-Resolved Raman spectra (raw data, no offset) of silicates, carbonates, phosphates and sulfates for the pristine sample out of the LIBS crater (green) and within the LIBS crater produced using 30 laser pulses (red). All spectra acquired for same analytical conditions and rescaled for better clarity by comparison with Gypsum 1 and Apatite OH by a multiplying factor as indicated.

Figure 3: Remote Time-Resolved Raman spectra (raw data, no offset) obtained at 8 meters in SuperCam-like configuration on different targets: [(a): orthopyroxenite, (b) hydromagnesite, (c) hematite, (d) pyrite]. For each sample, the green spectrum is collected on the pristine sample surface, the blue spectrum is centered on a 30-shots LIBS crater and the red spectrum is centered on a 100-shots LIBS crater.

Figure 4: (a) SEM image (Back-scattering electrons mode) of a 30-shots LIBS crater in ilmenite. The limits of the crater are outlined in red and were drawn by carefully considering the microtexture appearance of the sample as illustrated in (b) and (c). (b) Zoom within the LIBS crater (localization with black inset on (a)). Note the molten-like microtexture of the sample. (c) Magnified view of the pristine sample surface outside of the LIBS crater. Note the brittle-like microtexture of the sample.

Figure 5: CW Raman spectra of the ilmenite target (raw data, spectra offset). The reference spectrum obtained on the pristine surface of the sample is depicted in green. Raman spectra obtained in the 30-shots LIBS crater in vacuum (red), Earth atmosphere (blue) and Mars atmosphere (black) are depicted and show the local amorphization of ilmenite in the LIBS crater (see text).

Figure 6: (a) SEM image (Back-scattering electrons mode) of a 30-shots LIBS crater in pyrite. The limits of the crater are outlined in red and were drawn by carefully considering the microtexture appearance of the sample as illustrated in (b) and (c). (b) Zoom within the LIBS crater (localization with black inset on (a)). Note the molten-like microtexture. (c) Zoom outside the LIBS crater. Note the brittle-like microtexture of the sample.

Figure 7: (a) CW Raman mapping of a LIBS crater (30 shots in Martian atmosphere) in a pyrite target with pyrite in green, modified pyrite in blue in the crater and elemental sulfur in red. (b) Representative CW Raman spectra (raw data, spectra offset) of pyrite (in green), modified pyrite where a new peak at 451 cm^{-1} appears (in blue) and elemental sulfur (in red) as observed on the Raman map in (a). (see text for further explanation).

Figure 8: (a) SEM image (Secondary Electrons mode) of a LIBS crater (30 shots in Martian atmosphere) on the hematite target. Note the molten-like appearance of the sample surface within the crater. (b) FIB-SEM image (In Lens mode) of the FIB foil excavation. (c) TEM imaging of a FIB foil collected into the 30-shots LIBS crater showing a 200 nm thick magnetite layer covering the original hematite. (d) Selected-area electronic diffraction pattern of the magnetite layer. The electron diffraction pattern is consistent with magnetite viewed along the (112) zone axis.

Figure 9: (a) CW Raman mapping of a LIBS crater (30 shots in Martian atmosphere) in the hematite target with hematite in blue, magnetite in green in the crater and a transition boundary with both hematite and magnetite in red around the crater. The black area in the LIBS crater indicates the position where the FIB section was excavated. (b) Representative Raman spectra (raw data, spectra offset) of hematite (in blue), magnetite (in green) and mixed hematite-magnetite (in red) as observed on the Raman map in (a).

Figure 10: CW Raman spectra (raw data, spectra offset) of (a) coal and (b) graphite. For both samples, the green spectrum is collected on the pristine sample surface and the red spectra are collected within a 30-shots LIBS crater. In the case of graphite, note the nearly complete amorphization in the LIBS crater as represented by the lowermost spectrum (see text for further details).

Figure 11: Temperature diagrams obtained by calculations using the formalism by Bechtel (1975) for a LIBS laser shot on hematite.

(a) Temperature-Depth diagram: Note that the calculated molten layer thickness of hematite is ≈1 micrometer (red vertical line) in reasonable agreement with the thickness of the magnetite layer observed by TEM (blue dashed line).

(b) Temperature-Time diagram: Temperatures higher than the melting temperature of hematite are maintained over a few hundreds of nanoseconds. At the ChemCam LIBS repetition rate (red arrow), cumulative effects from one laser pulse to the next are negligible.

Table captions:

Table 1: List of samples analyzed by LIBS and Raman spectroscopy with theoretical ideal formula, reference for relevance to Mars, origin and nature of the sample.

Table 2: Comparison of Raman (R_{signal}) and Background (R_{bkg}) intensities for spectra collected inside and outside the LIBS crater of reference minerals (see text) with micro TR Raman. Position of the most intense peak used for R_{signal} and spectral ranged used for R_{bkg} are indicated. +/- means increase/decrease of the ratio by a factor in the range 1 to 2, + +/- - in the range 2 to 5, + + +/- - - higher than 5. (p): pellet samples.

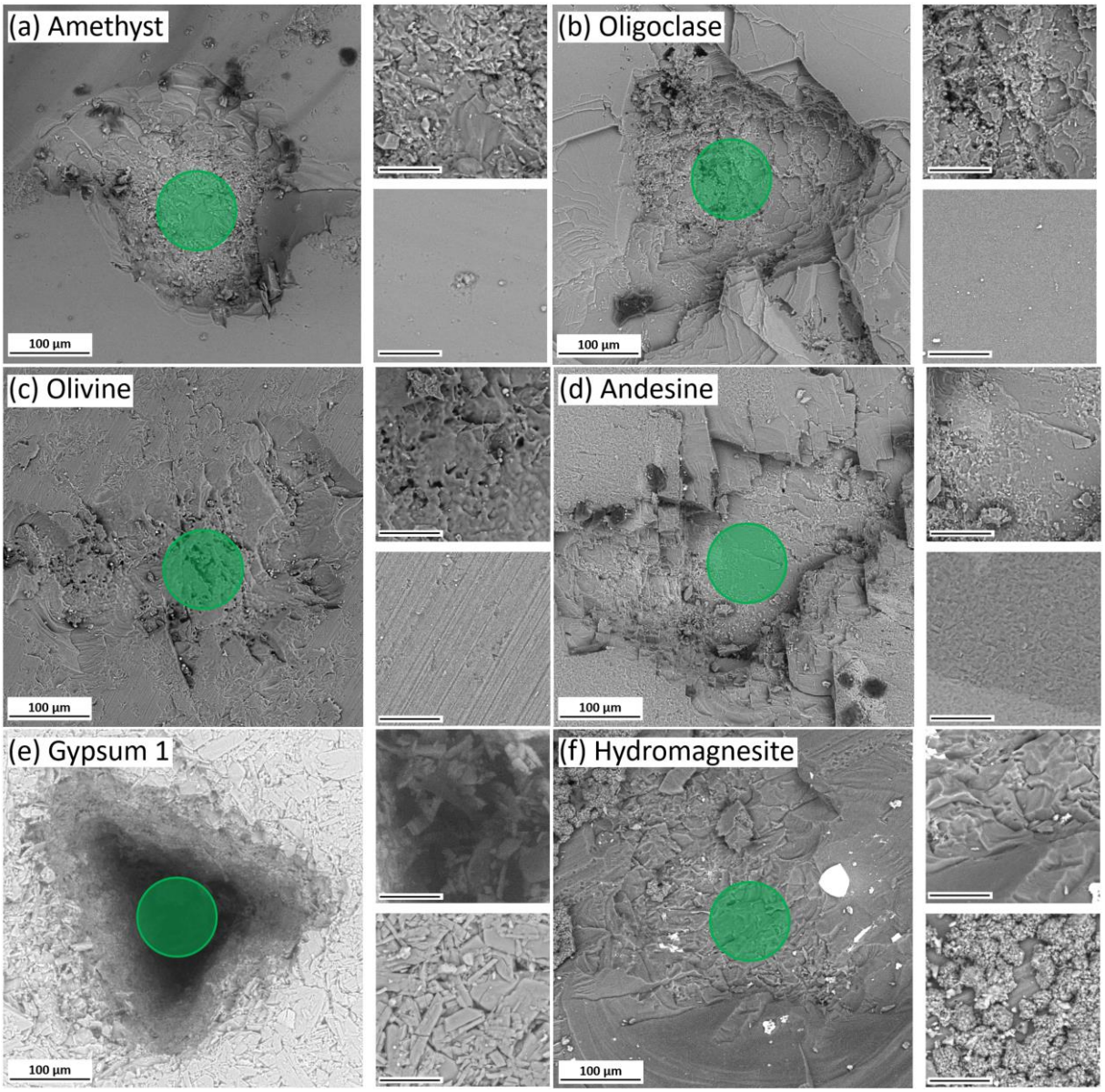

Figure 1: SEM images of some representative LIBS craters for silicates, carbonates, phosphates and sulfates minerals obtained in backscattered electrons mode. Samples represented are: (a) amethyst, (b) oligoclase, (c) olivine, (d) andesine, (e) gypsum 1, (f) hydromagnesite. For each example, the large image (left) depicts the whole crater, the top small image on the right side depicts the sample surface within the LIBS crater and the bottom small image on the right side depicts the pristine sample surface out of the crater. Scale bars indicate 100 µm for each large image and 40 µm for each small image. The 90 µm laser spot diameter for micro time-resolved Raman spectroscopy is sketched in green.

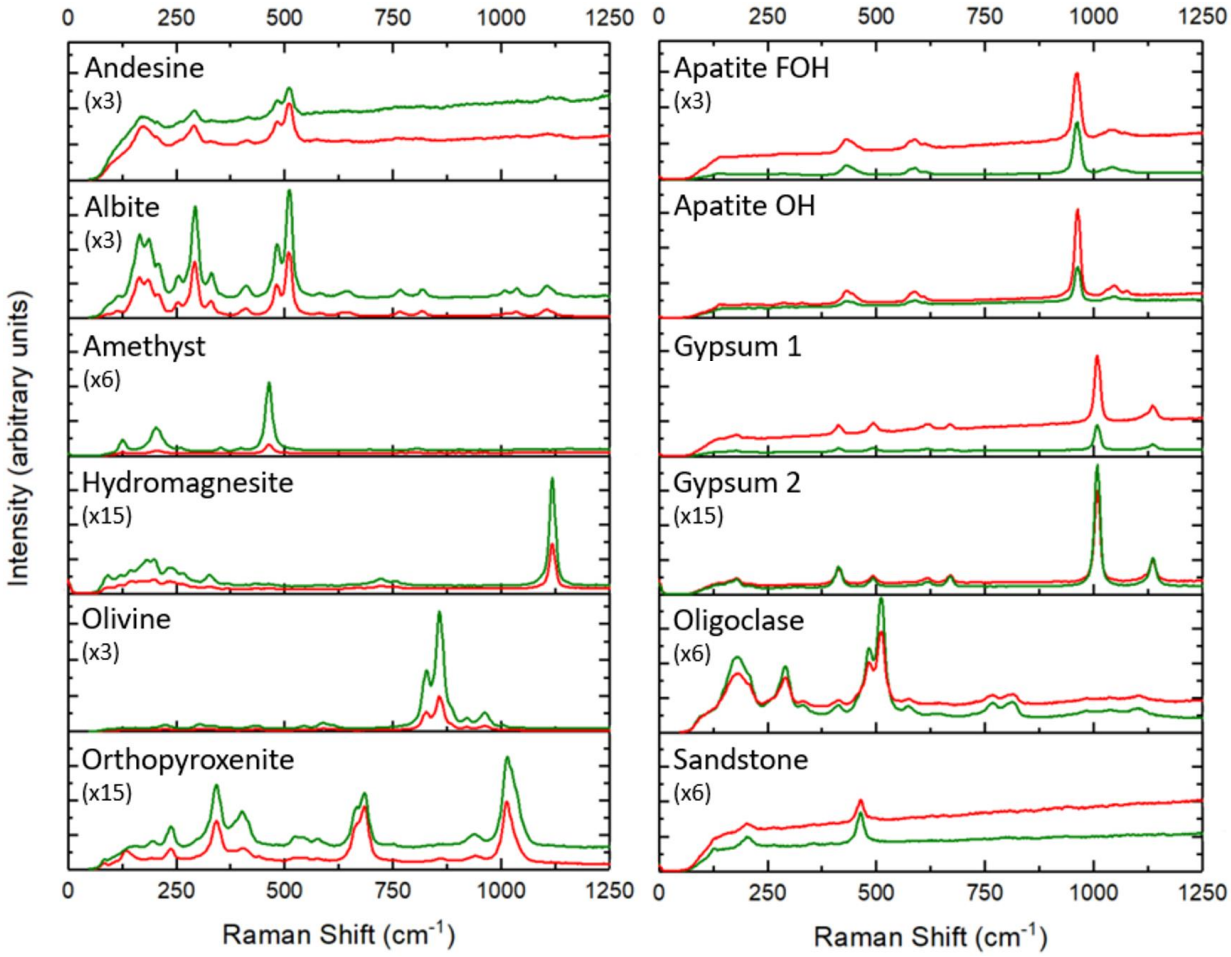

Figure 2: Micro Time-Resolved Raman spectra (raw data, no offset) of silicates, carbonates, phosphates and sulfates for the pristine sample out of the LIBS crater (green) and within the LIBS crater, produced using 30 laser pulses (red). All spectra acquired for same analytical conditions and rescaled for better clarity by comparison with Gypsum 1 and Apatite OH by a multiplying factor as indicated.

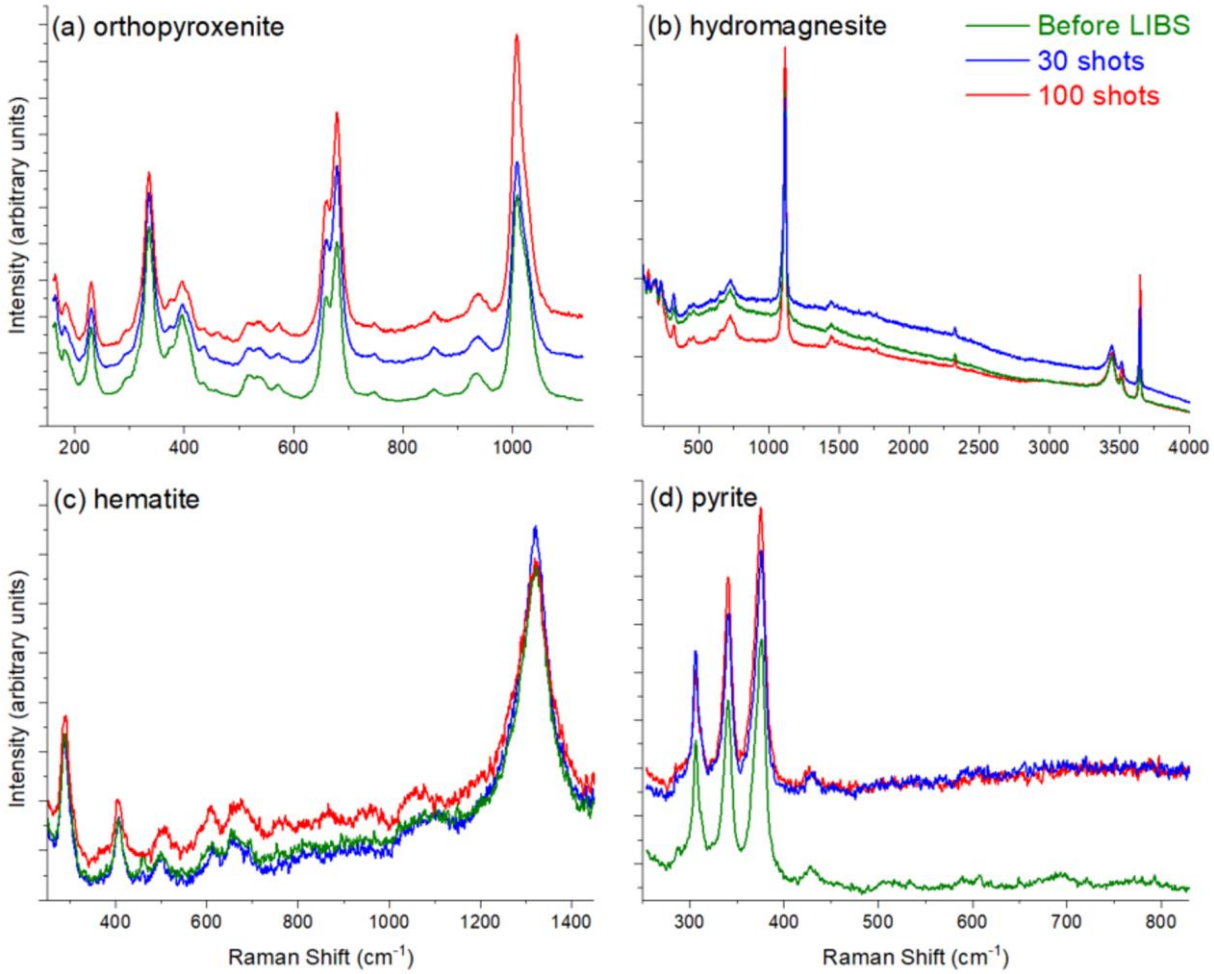

Figure 3: Remote Time-Resolved Raman spectra (raw data, no offset) obtained at 8 meters in SuperCam-like configuration on different targets: [(a): orthopyroxenite, (b) hydromagnesite, (c) hematite, (d) pyrite]. For each sample, the green spectrum is collected on the pristine sample surface, the blue spectrum is centered on a 30-shots LIBS crater and the red spectrum is centered on a 100-shots LIBS crater.

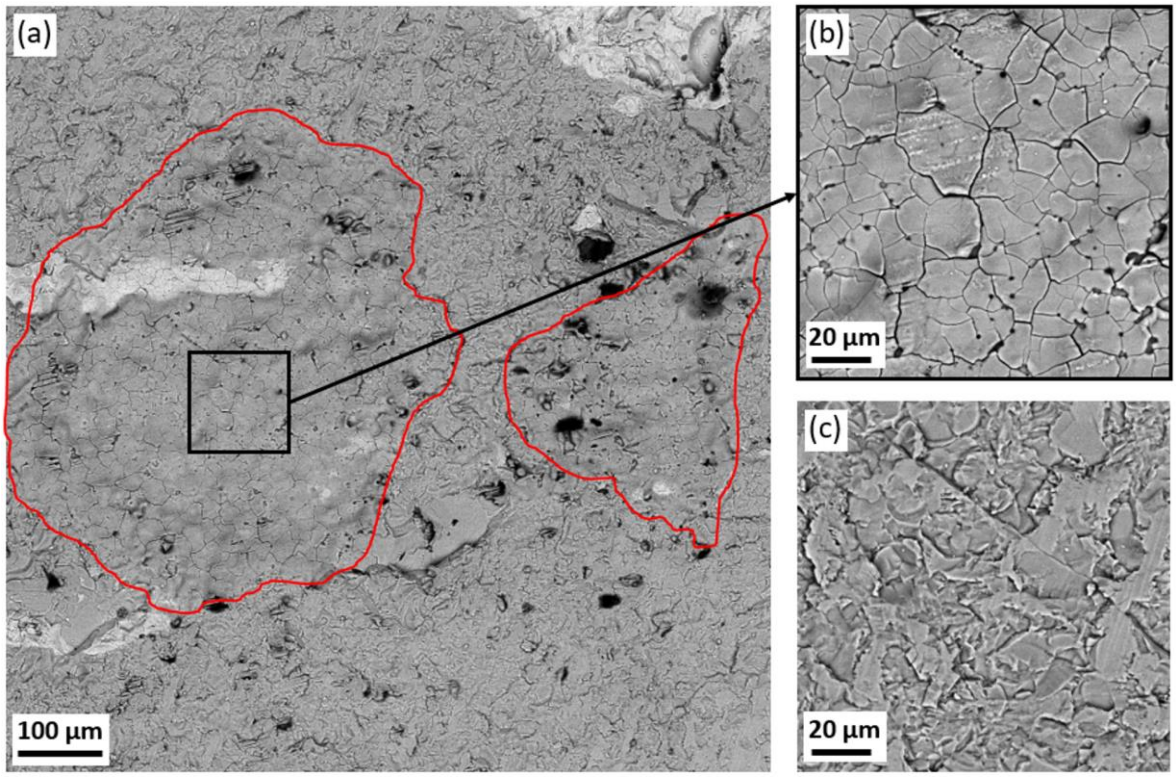

Figure 4: (a) SEM image (BSE mode) of a 30-shot LIBS crater in ilmenite. The limits of the crater are outlined in red and were drawn by carefully considering the microtexture appearance of the sample as illustrated in (b) and (c). (b) Zoom within the LIBS crater (localization with black inset on (a)). Note the molten-like microtexture of the sample. (c) Magnified view of the pristine sample surface outside of the LIBS crater. Note the brittle-like microtexture of the sample.

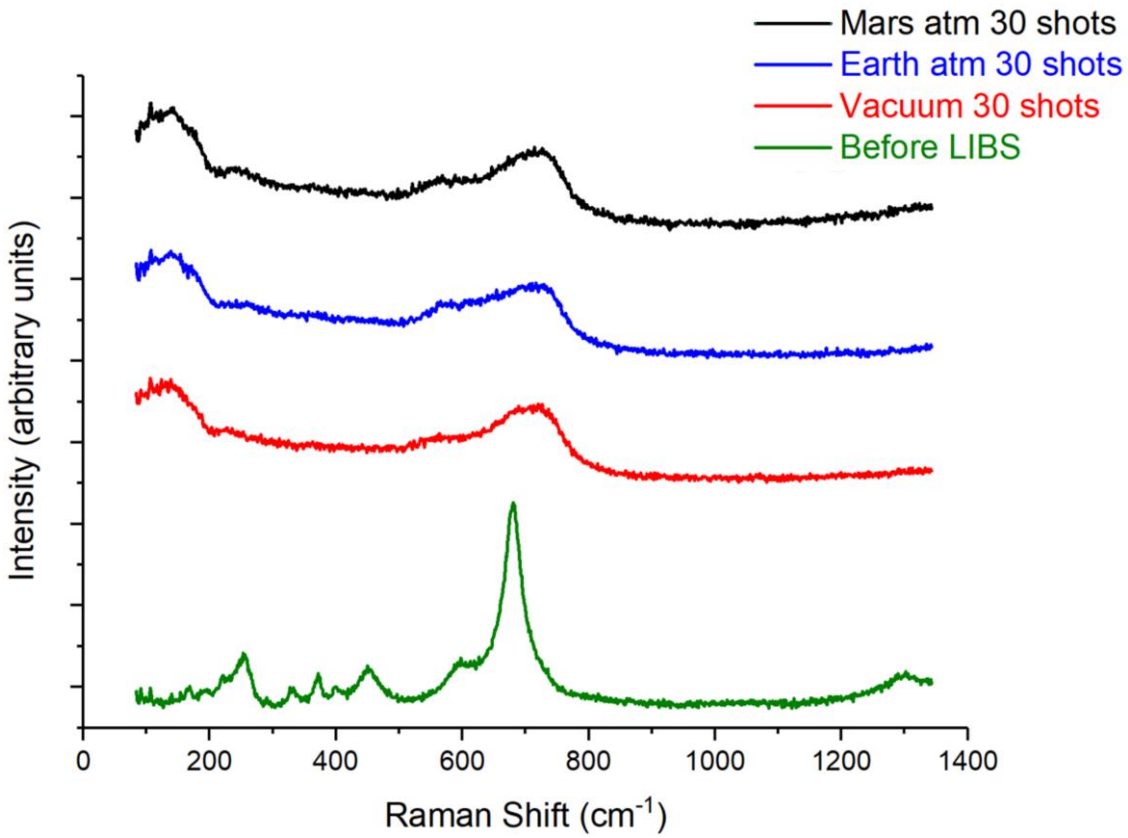

Figure 5: CW Raman spectra of the ilmenite target (raw data, spectra offset). The reference spectrum obtained on the pristine surface of the sample is depicted in green. Raman spectra obtained in the 30-shots LIBS crater in vacuum (red), Earth atmosphere (blue) and Mars atmosphere (black) are depicted and show the local amorphization of ilmenite in the LIBS crater (see text).

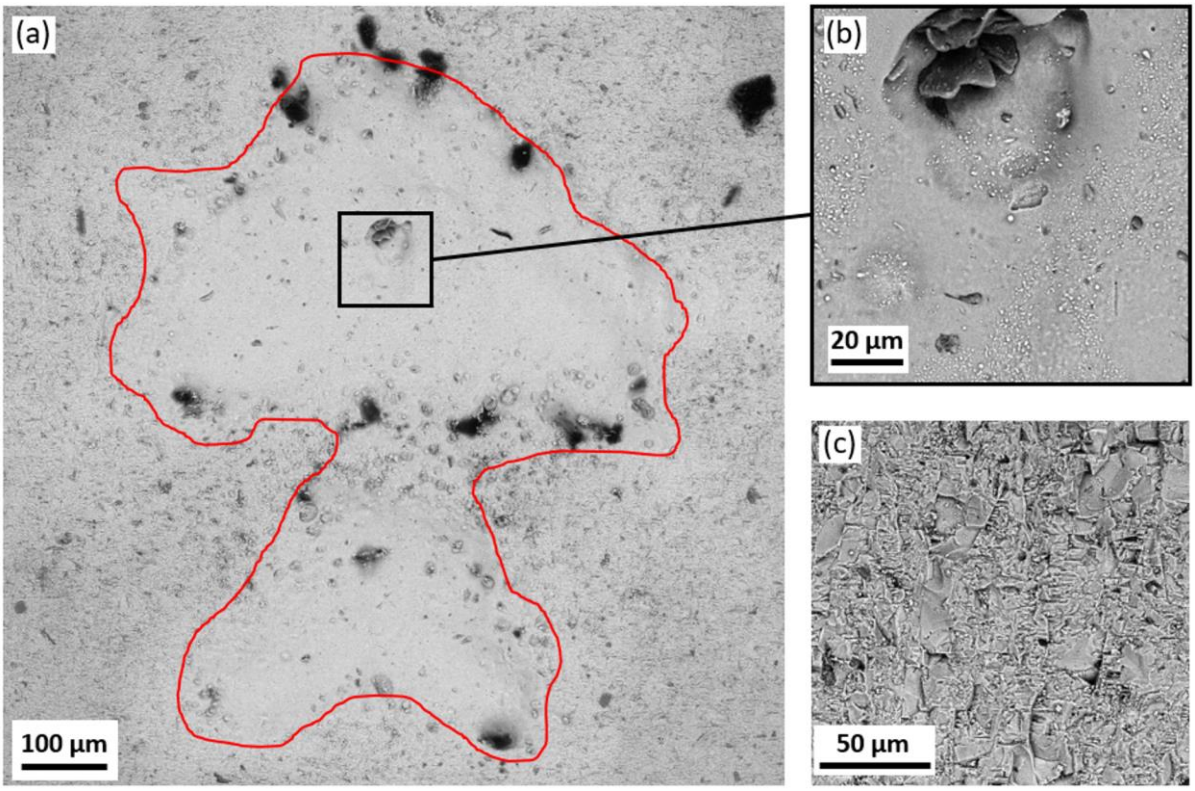

Figure 6: (a) SEM image (Back-scattering electrons mode) of a 30-shots LIBS crater in pyrite. The limits of the crater are outlined in red and were drawn by carefully considering the microtexture appearance of the sample as illustrated in (b) and (c). (b) Zoom within the LIBS crater (localization with black inset on (a)). Note the molten-like microtexture. (c) Zoom outside the LIBS crater. Note the brittle-like microtexture of the sample.

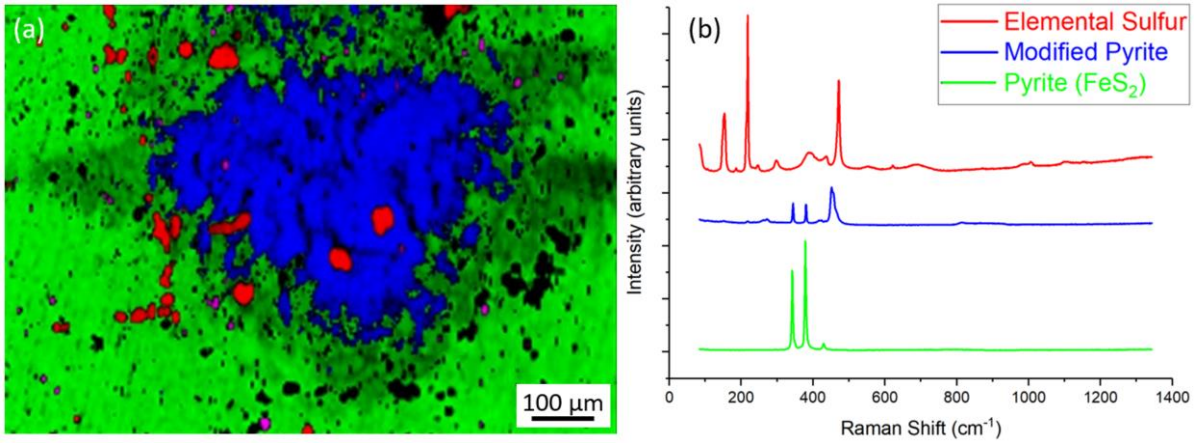

Figure 7: (a) CW Raman mapping of a LIBS crater (30 shots in Martian atmosphere) in a pyrite target with pyrite in green, modified pyrite in blue in the crater and elemental sulfur in red. (b) Representative CW Raman spectra (raw data, spectra offset) of pyrite (in green), modified pyrite where a new peak at 451 cm^{-1} appears (in blue) and elemental sulfur (in red) as observed on the Raman map in (a). (see text for further explanation).

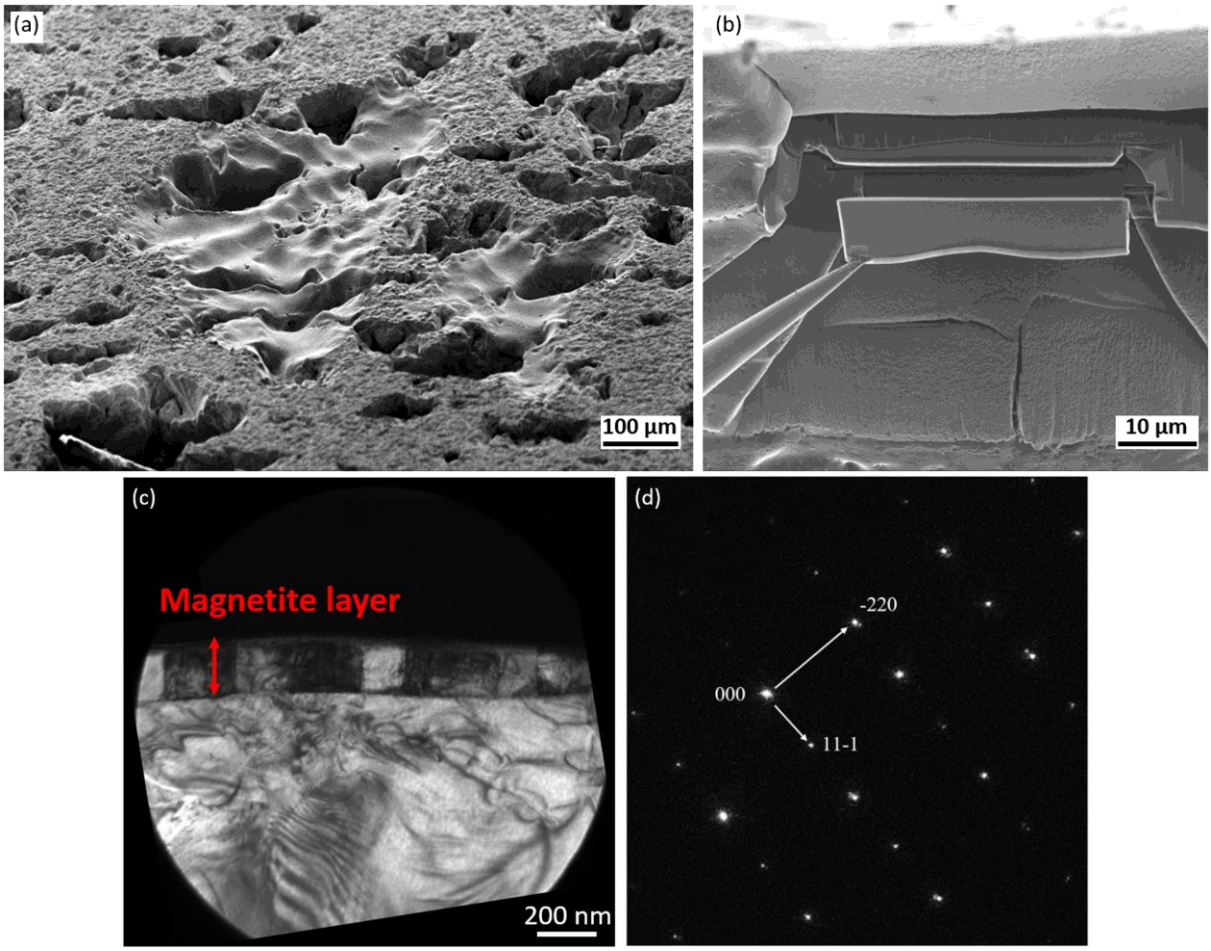

Figure 8: (a) SEM image (Secondary Electrons mode) of a LIBS crater (30 shots in Martian atmosphere) on the hematite target. Note the molten-like appearance of the sample surface within the crater. (b) FIB-SEM image (In Lens mode) of the FIB foil excavation. (c) TEM imaging of a FIB foil collected into the 30-shots LIBS crater showing a 200 nm thick magnetite layer covering the original hematite. (d) Selected-area electronic diffraction pattern of the magnetite layer. The electron diffraction pattern is consistent with magnetite viewed along the (112) zone axis.

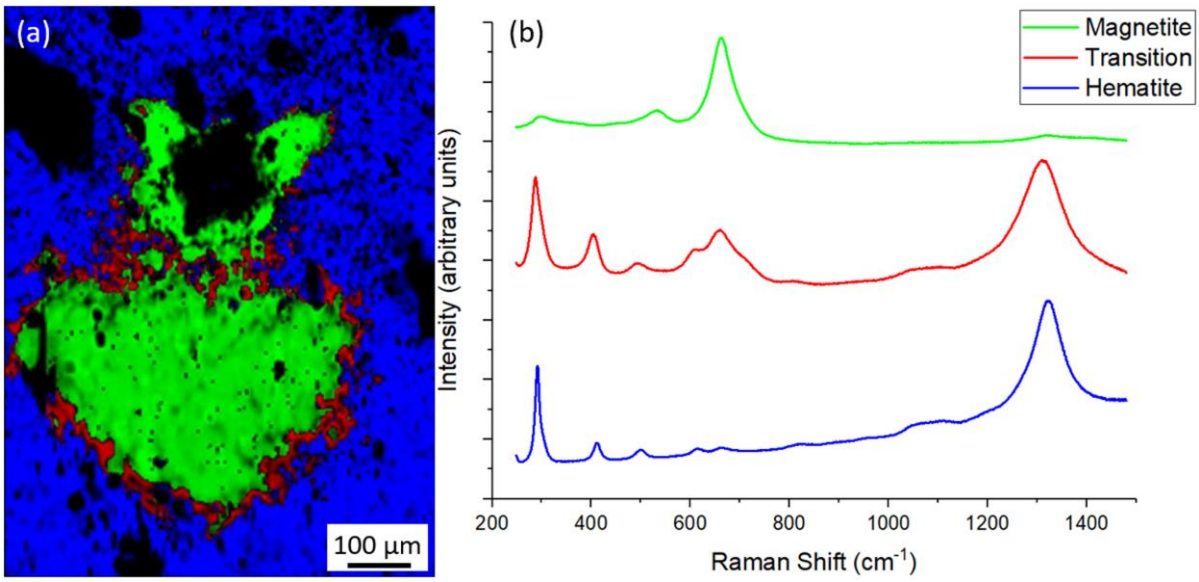

Figure 9: (a) CW Raman mapping of a LIBS crater (30 shots in Martian atmosphere) in the hematite target with hematite in blue, magnetite in green in the crater and a transition boundary with both hematite and magnetite in red around the crater. The black area in the LIBS crater indicates the position where the FIB section was excavated. (b) Representative Raman spectra (raw data, spectra offset) of hematite (in blue), magnetite (in green) and mixed hematite-magnetite (in red) as observed on the Raman map in (a).

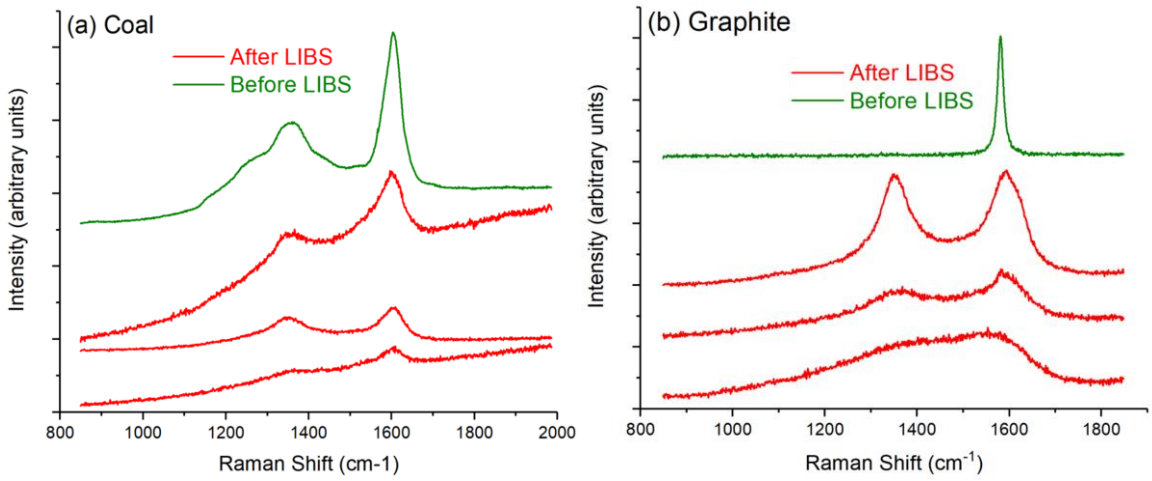

Figure 10: CW Raman spectra (raw data, spectra offset) of (a) coal and (b) graphite. For both samples, the green spectrum is collected on the pristine sample surface and the red spectra are collected within a 30-shots LIBS crater. In the case of graphite, note the nearly complete amorphization in the LIBS crater as represented by the lowermost spectrum (see text for further details).

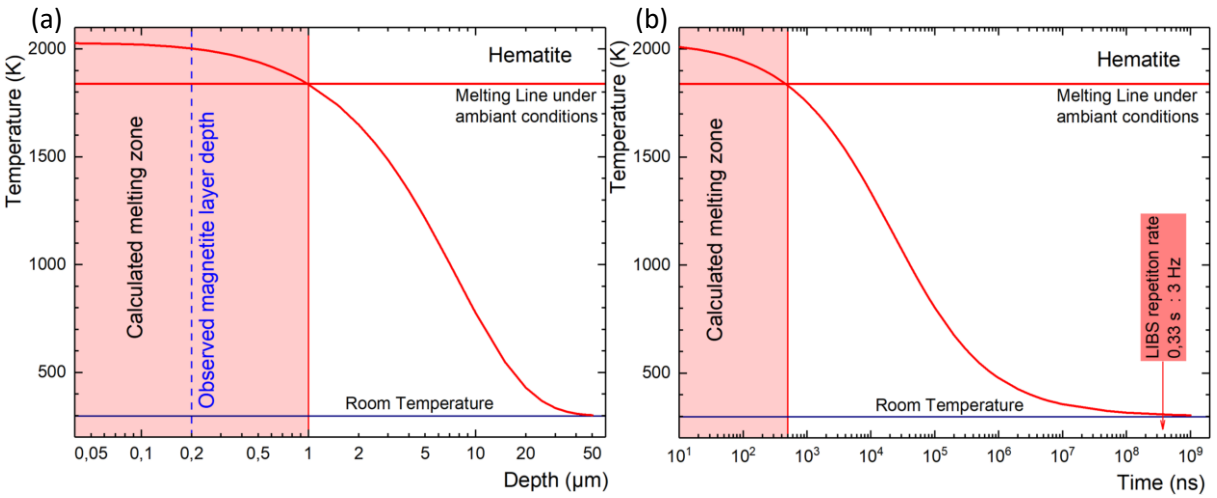

Figure 11: Temperature diagrams obtained by calculations using the formalism by Bechtel (1975) for a LIBS laser shot on hematite.

(a) Temperature-Depth diagram: Note that the calculated molten layer thickness of hematite is ≈1 micrometer (red vertical line) in reasonable agreement with the thickness of the magnetite layer observed by TEM (blue dashed line).

(b) Temperature-Time diagram: Temperatures higher than the melting temperature of hematite are maintained over a few hundreds of nanoseconds. At the ChemCam LIBS repetition rate (red arrow), cumulative effects from one laser pulse to the next are negligible.

Sample	**Ideal formula**	**Mars reference**	**Origin**	**Nature**
Amethyst	SiO_2	[59]	Unknown	Crystal
Sandstone	SiO_2 (> 98,5%)	[59]	Fontainebleau (France)	Powder pellet
Albite	$NaAlSi_3O_8$	[60]	Alps (France)	Crystal
Olivine	$(Mg,Fe)_2[SiO_4]$	[61,62,63]	San Carlos (USA)	Crystal
Orthopyroxenite	$(Mg,Fe)_2Si_2O_6$	[59,63,64]	Zimbabwe	Natural rock
Oligoclase	$(Na,Ca)[Al(Si,Al)Si]_2O_8$	[60]	Sweden	Crystal
Andesine	$(Ca,Na)(Al,Si)_4O_8$	[60,65]	Unknown	Crystal
Calcite	$CaCO_3$	[66]	Alfa Aesar	Powder pellet
Hydromagnesite	$Mg_5(CO3)_4(OH)_2 \cdot 4H_2O$	[66]	Iran	Crystal
Apatite, FOH	$Ca_{10}(PO_4)_6F(OH)$	[59,65,67]	Synthetic	Powder pellet
Apatite, OH	$Ca_{10}(PO_4)_6(OH)_2$	[59,65,67]	Synthetic	Powder pellet
Gypsum 1	$Ca(SO_4) \cdot 2H_2O$	[68,69]	Aldrich	Powder pellet
Gypsum 2	$Ca(SO_4) \cdot 2H_2O$	[68,69]	Volterra, Italy	Crystal
Graphite	C	[70]	Madagascar	Crystal
Coal	Includes C, H, O, N	[70]	Cévennes (France)	Powder Pellet
Pyrite	FeS_2	[65,71,72]	Navajun (Spain)	Crystal
Ilmenite	$FeTiO_3$	[63,65]	Kragerø (Norway)	Crystal
Hematite	Fe_20_3	[59,73]	Elba (Italy)	Crystal

Table 1: List of samples analyzed by LIBS and Raman spectroscopy with theoretical ideal formula, reference for relevance to Mars, origin and nature of the sample.

Sample	Most intense Raman peak (cm^{-1})	R_{bkg} range (cm^{-1})	R_{bkg}	R_{signal}
Andesine	507	550-850	-	+
Albite	507	540-740	- - -	-
Amethyst	464	540-740	-	- - -
Hydromagnesite	1120	850-1050	-	- -
Olivine	855	1000-1200	- -	- -
Orthopyroxenite	1008	720-920	- -	-
Calcite (p)	1086	750-1050	- -	-
Apatite FOH (p)	961	700-900	+ + +	+
Apatite OH (p)	962	700-900	+	+ +
Gypsum 1 (p)	1008	750-950	+ + +	+ +
Gypsum 2	1008	750-950	+	-
Oligoclase	509	590-790	+ +	-
Sandstone (p)	465	600-900	+	-

Table 2: Comparison of Raman (R_{signal}) and Background (R_{bkg}) intensities for spectra collected inside and outside the LIBS crater of reference minerals (see text) with micro TR Raman. Position of the most intense peak used for R_{signal} and spectral ranged used for R_{bgk} are indicated. +/- means increase/decrease of the ration by a factor in the range [1;2], + +/- - in the range [2;5], + + +/- - - higher than 5. (p): pellet samples.